Acta Mech
https://doi.org/10.1007/s00707-018-2355-4

CrossMark

ORIGINAL PAPER

Diego Dotto · Cristian Marchioli

Orientation, distribution, and deformation of inertial flexible fibers in turbulent channel flow

Received: 17 August 2018 / Revised: 19 December 2018

Abstract In this paper, we investigate the dynamics of flexible fibers in turbulent channel flow. Fibers are longer than the Kolmogorov length scale of the carrier flow, and their velocity relative to the surrounding fluid is non-negligible. Our aim is to examine the effect of local shear and turbulence anisotropy on the translational and rotational behavior of the fibers, considering different elongation (parameterized by the aspect ratio, λ) and inertia (parameterized by the Stokes number, St). To these aims, we use a Eulerian–Lagrangian approach based on direct numerical simulation of turbulence in the dilute regime. Fibers are modeled as chains of sub-Kolmogorov rods (referred to as elements hereinafter) connected through ball-and-socket joints that enable bending and twisting under the action of the local fluid velocity gradients. Velocity, orientation, and concentration statistics, extracted from simulations at shear Reynolds number $Re_\tau = 150$ (based on the channel half height), are presented to give insights into the complex fiber–turbulence interactions that arise when non-sphericity and deformability add to inertial bias. These statistical observables are examined at varying aspect ratios (namely $\lambda_r = l_r/a = 2$ and 5, with l_r the semi-length of each rod-like element r composing the fiber and a its cross-sectional radius) and varying fiber inertia (considering values of the element Stokes number, $St_r = 1, 5, 30$). To highlight the effect of flexibility, statistics are compared with those obtained for fibers of equal mass that translate and rotate as rigid bodies relative to the surrounding fluid. Flexible fibers exhibit a stronger tendency to accumulate in the very-near-wall region, where they appear to be trapped by the same inertia-driven mechanisms that govern the preferential concentration of spherical particles and rigid fibers in bounded flows. In such region, the bending of flexible fibers increases as inertia decreases, and fiber deformation appears to be controlled by mean shear and turbulent Reynolds stresses. Preferential segregation into low-speed streaks and preferential orientation in the mean flow direction is also observed.

List of symbols

$\underline{a}$	Fiber radius
$\bar{\mathbf{A}}$	Drag force resistance tensor
C_D	Drag coefficient
e_c	Equivalent fiber eccentricity
$\mathbf{F}^D$	Hydrodynamic drag force
h	Channel half height
$\mathbf{H}^D$	Hydrodynamic drag torque due to fluid velocity gradients

D. Dotto · C. Marchioli (✉)
Department of Engineering and Architecture, University of Udine, 33100 Udine, Italy
E-mail: marchioli@uniud.it

C. Marchioli
Department of Fluid Mechanics, CISM, Piazza Garibaldi 18, 33100 Udine, Italy

Published online: 11 January 2019

$\bar{\bar{\mathbf{J}}}$	Inertia tensor
l_r	Semi-length of one fiber element
L	End-to-end distance
L_f	Lenght of the entire fiber
m_p	Mass of the fiber
$\mathcal{N}$	Number of elements per fiber
$\mathbf{o}$	Orientation vector
$\mathcal{P}$	Pressure
$\mathbf{p}$	Position vector
Re	Reynolds number
St	Stokes number
t	Time
S	Fiber-to-fluid density ratio
$\mathbf{T}^D$	Hydrodynamic drag torque due to the action of the fluid vorticity on the element
$\mathbf{u}$	Fluid velocity
$\mathbf{v}$	Fiber velocity
x	Streamwise direction
$\mathbf{X}$	Constraint force
y	Spanwise direction
z	Wall-normal direction

Greek letters

α	Solid angle between neighboring fiber elements
δ_{VS}	Viscous sublayer thickness
$\bar{\bar{\boldsymbol{\delta}}}$	Identity matrix
Δt	Time step
$\bar{\bar{\bar{\boldsymbol{\epsilon}}}}$	Levi-Civita tensor
$\bar{\bar{\boldsymbol{\gamma}}}$	Fluid velocity gradient tensor
λ	Aspect ratio
μ	Fluid dynamic viscosity
ρ	Fluid density
ν	Fluid kinematic viscosity
$\boldsymbol{\omega}$	Fiber angular velocity
$\boldsymbol{\Omega}$	Fluid angular velocity

1 Introduction

The motion of non-spherical particles in turbulent flow is a complex problem that has received growing attention in the last decade. Complexity arises primarily from the multiscale nature of turbulence and from the coupling between the translational and rotational dynamics of the particles, which are governed by forces and torques that depend on particle shape and orientation [66]. The interest in tackling such a challenging problem comes from its many applications in both industry (e.g., pulp and paper making [14,33,59], post-combustion soot emission [41], food or pharmaceutical processing [4]) and environment (e.g., atmospheric dispersion of pollen [52], plankton dynamics in water bodies [12,31] or ice crystal formation in clouds [20]).

From a numerical point of view, several models are available to describe translation and rotation of non-Brownian non-spherical particles in fluid flows (see [66] for a review). The most natural approach to investigating particle–turbulence interaction at the particle scale relies on the Eulerian description of turbulence and on the Lagrangian description of particle trajectories [63]. Within this approach, the simplest model is based on the assumption that particles behave as perfect flow tracers: In this limit, namely when the particle Reynolds number is much smaller than unity (or equal to zero, ideally), exact equations for the time evolution of particle orientation are available for both axisymmetric [23] and non-axisymmetric particles [21]. This approach has proven useful to study the motion of elongated micro-swimmers and non-motile plankton cells in turbulence [31,32,42,77].

When the particle Reynolds number is small but the translational and rotational slip between the particle and fluid cannot be neglected, dynamical equations of rigid body motion can be used in which expressions for forces and torques acting on the particle are available for simple shapes (in particular, prolate and oblate spheroids) [5,6,19,66]. This approach has been used to study the motion of rigid ellipsoids and disks in viscous and turbulent flow [9,36,37,55,72–74,76]. If the particle Reynolds number becomes order unity or larger, then the combined effect of fluid and particle inertia should be taken into account [29]. This effect has been examined for many different shapes in steady simple shear flow or isotropic turbulence [8,29,49,60] but remains largely unexplored in unsteady anisotropic flows. Empirical correlations are available, yet not applicable across the full range of spheroidal shapes [66].

When particles have at least one dimension larger than (or comparable to) the Kolmogorov scale but are not in the slender body limit, fully resolved simulations have become feasible (see [40,67]) in view of the exponential increase in computational resources, which allows accurate tracking of the particles upon integration of fluid forces on the particle surface. As far as non-spherical particles in turbulence are concerned, however, studies based on fully resolved simulations have focused primarily on spherical particles, with only few applications to elongated (and rigid) particles in channel flow: Do-Quang et al. [15] simulated $\mathcal{O}(10^4)$ cylindrical fibers with size equivalent to a few grid cells up to 0.4% volume fraction; Niazi-Ardekani et al. [43] performed DNS of suspensions of oblate spheroids using the immersed boundary method, which was also employed by Eshghinejadfard et al. [16] to examine spheroids with aspect ratio up to 4 and solid-phase volume fractions between 0.75 and 1.5%. These studies provide insights into the mechanisms that govern particle-induced turbulence modulation, revealing drag reduction in flows laden with oblate spheroids [43] and drag increase in flows laden with prolate spheroids [16]. A rather large body of literature is available for studies dealing with the analysis of fluid–structure interactions in the presence of flexible filaments (see [22,45,62,79] among others), but an analysis of this problem is beyond the scope of the present paper.

Most of the numerical studies in which the above-mentioned models have been applied to non-spherical particles in turbulence focus on the case of rigid, non-deformable spheroids. The Jeffery equation [23], which describes exactly the periodical motion of an isolated prolate spheroid in simple shear flow, and its extensions to arbitrary flow fields [5,6] and to non-axisymmetric ellipsoids [21] have been the foundation to study the motion of rigid inertialess fibers. However, the Jeffery equations cannot be used to describe bending and twisting of long flexible fibers: Such fibers may execute a Jeffery orbit in the initial stages of motion but this orbit is not a stable one and will eventually drift through orbital constants [24]. As far as inertial (rigid and elongated) particles in turbulence are concerned, their translational and rotational dynamics has been often investigated using a micro-hydrodynamic approach combining a large number of particles into a multi-rigid-body system. In this case, the physical problem investigated involved the dispersion of fibers and disks with length much smaller that the flow domain in fully developed turbulence [2]. For such a problem, the adoption of a micro-hydrodynamic approach based on accurate direct numerical simulation of the flow, combined with recent experimental measurements [51], has led to a fairly good understanding of shape and size effects on macroscopic phenomena such as preferential concentration and wall accumulation in dilute suspensions (see [66] for a review).

Besides particle shape and size, however, one additional feature that is relevant to applications and still to be grounded in fundamental physics is particle deformability, namely the tendency of very elongated (high aspect ratio) particles, referred to as fibers hereinafter, to flexure under the action of the underlying flow field. Flexible fibers are commonly found both in low-Reynolds-number flows (e.g., polymers, proteins or other biological systems [30,57,79]) and in high-Reynolds-number flows (e.g., in the processing of fiber-reinforced composite materials [78], in pulp and paper making [33,64] or hydro-entanglement processes [70]). Clearly, these fibers introduce an additional geometrical complexity associated with their irregular shape, which has important consequences on the rheological properties and microstructure of the suspension [69]. While the interaction of flexible fibers with fluid flow at low Reynolds number has been examined in several theoretical and numerical works [47,57,61,68], aimed at understanding buckling instabilities, topological changes in fiber shape and bending mode transition criteria, the effect of flexibility on turbulent suspensions at high Reynolds number has been poorly investigated. Recently, a series of experiments have been performed by Verhille and co-workers [7,65] to understand the importance of fiber deformation on its transport in homogeneous isotropic turbulence: In these experiments, fibers with length up to the integral timescale of the flow were considered and a critical length (the elastic length) was identified, above which flexibility cannot be neglected.

To the best of our knowledge, however, there are very few numerical simulations dealing with flexible fibers in a fully developed, three-dimensional and time-dependent turbulent flow. Andríc et al. [2] studied the translation and re-orientation of fibers in turbulent channel flow and found that fibers exhibit complex geometrical configurations during their motion, similar to conformations of polymer strands subject to thermal fluctuations. More recently, Kunhappan et al. [26] examined the motion of flexible fibers in both homogeneous isotropic turbulence, considering flow conditions and fiber parameters similar to those of [65], and channel flow turbulence, considering a 1% concentration fiber suspension with fixed fiber-to-fluid density ratio. For the purposes of the present study, these works are of particular relevance, since we are interested in the dynamics of flexible fibers in wall-bounded turbulent flow. In particular, we focus on fibers that are longer than the Kolmogorov scale but much smaller than the flow domain. To study this problem, several micro-hydrodynamic approaches, which differ for the mathematical model employed to represent the fiber, have been proposed. The first model was put forth by Matsuoka and Yamamoto [71]: The fiber is modeled as a chain of spherical beads (hence the name bead-chain model) in which each bead obeys a kinematic constraint that prevents detachment of neighboring beads while allowing for relative rotation. This model has been used recently by Delmotte et al. [13] to study self-propelling filaments in viscous flow and by Sasayama et al. [53] to study fiber motion during processing of fiber-reinforced thermoplastics. A modified version of the bead-chain model was later proposed by Ross and Klingenberg [50], who used a chain of rigid ellipsoids, and by Schmid et al. [54], who represented each element in the chain as a massless, rigid, cylindrical segment. This latter model was extended to inertial fibers by Lindström and Uesaka [28], who derived an approximate model for the interaction between fiber elements and the surrounding fluid at finite element Reynolds number, and accounted for long-range hydrodynamic interactions between fibers. The model was used by the same authors to study paper forming [27] and later by Martínez et al. [39] to study clustering of long flexible fibers in 2D Arnold–Beltrami–Childress flow and by Andríc et al. [2,3] to study fiber–flow interactions and rheological properties of dilute suspensions in channel flow turbulence.

In the present paper, we build on the work of Andríc et al. [2] and of Kunhappan et al. [26] and develop a comprehensive database of fiber trajectories, velocities and orientations to examine how flexibility adds to fiber elongation and inertia in determining fiber translation, rotation, and spatial distribution within the flow. Compared to [2], in particular, we use Reynolds-number-dependent expressions for the drag coefficient (instead of assuming it constant) and we consider much longer simulations (to reach a steady state for fiber concentration), a much higher number of fibers (10^5 instead of 50 in the same computational domain), higher fiber-to-fluid density ratios and higher fiber length-to-channel height ratios.

2 Physical problem and methodology

2.1 Flow field

The reference flow configuration chosen to simulate wall shear turbulence is Poiseuille flow of incompressible, isothermal, and Newtonian fluid in a plane channel. Conservation of mass and momentum of the fluid is described by the following set of three-dimensional time-dependent equations, written in dimensionless vector form:

$$\nabla \cdot \mathbf{u} = 0\,; \tag{1}$$

$$\frac{\partial \mathbf{u}}{\partial t} + \mathbf{u} \cdot \nabla \mathbf{u} = -\nabla \mathcal{P} + \frac{1}{Re_\tau} \nabla^2 \mathbf{u} \tag{2}$$

where $\mathbf{u} = (u_x, u_y, u_z)$ is the fluid velocity, and $\nabla \mathcal{P}$ is the imposed pressure gradient that drives the flow in the streamwise direction. We performed direct numerical simulation (DNS) of these equations, imposing periodic boundary conditions in the streamwise (x) and spanwise (y) directions and no-slip conditions at the walls.

2.2 Fiber tracking

Lagrangian fiber dynamics is treated in the same way as in [28,54]. The reader is referred to these articles for a detailed description of the fiber model. Here, we provide only the main features of the model. Each fiber is modeled as a chain of $\mathcal{N}$ rigid and inextensible elements of circular cross section, indexed $r \in [1, \mathcal{N}]$. Fiber elements have the same diameter and length and are connected together by $\mathcal{N} - 1$ hinges, as shown in Fig. 1. The location of each element is given with respect to a inertial frame of reference that uses a Cartesian coordinate system, with axes defined by the base vectors $\{\mathbf{e}_x, \mathbf{e}_y, \mathbf{e}_z\}$ and origin denoted by O. Each fiber element is subject to hydrodynamic interactions, determined by the action of the drag force and torques, but

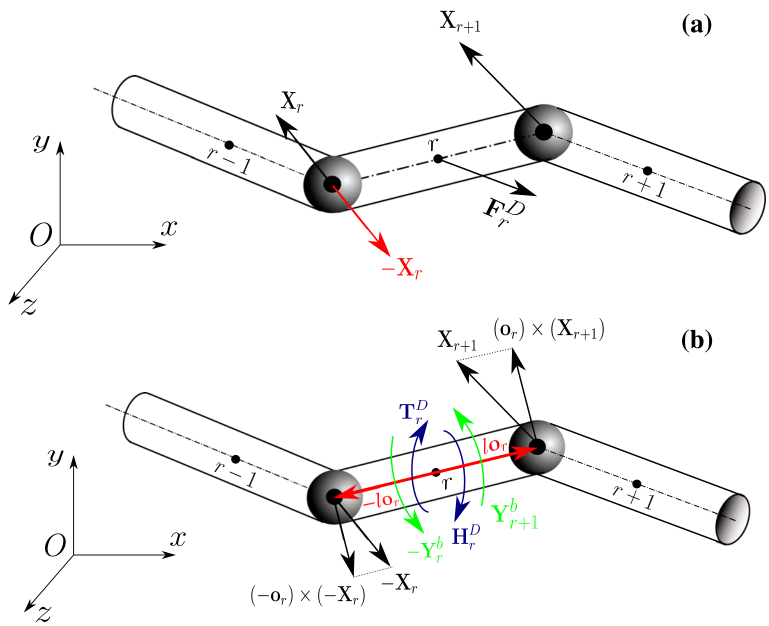

Fig. 1 Forces (**a**) and torques (**b**) applied on the rth element of the fiber

also to interactions with its neighbors due to the connectivity constraint, which ensures that end points of adjacent elements coincide: The resulting contact forces preserve the integrity of the fiber by allowing relative rotation of adjacent elements, yet not relative translation (Fig. 2).

The motion of the rth fiber element [28,54] with density ρ_p and aspect ratio $\lambda_r = l_r/a$, a being its cross-sectional radius, is governed by Euler's first and second equations of motion and by the connectivity constraint. In vector form, these read as:

$$m_p \frac{d\mathbf{v}_r}{dt} = \mathbf{F}_r^D + \mathbf{X}_{r+1} - \mathbf{X}_r; \tag{3}$$

$$\frac{d\left(\bar{\bar{\mathbf{J}}}_r \boldsymbol{\omega}_r\right)}{dt} = \mathbf{T}_r^D + \mathbf{H}_r^D + l_r \boldsymbol{o}_r \times (\mathbf{X}_{r+1} + \mathbf{X}_r)\,; \tag{4}$$

$$\boldsymbol{\Psi} = \mathbf{p}_r + l_r \mathbf{o}_r - (\mathbf{p}_{r+1} - l_{r+1}\mathbf{o}_{r+1}) = \mathbf{0}. \tag{5}$$

In Eq. (3), $m_p = \rho_p 2\pi \lambda_r a^3$ is the mass of the element; $\mathbf{v}_r$ is the translational velocity of its center of mass; $\mathbf{F}_r^D$ is the hydrodynamic drag force exerted by the surrounding fluid. Terms $\mathbf{X}_{r+1}$ and $\mathbf{X}_r$ are the constraint forces produced by element $r+1$ on element r and by element r on element $r-1$, respectively.

In Eq. (4), $\bar{\bar{\mathbf{J}}}_r = \frac{m_p a^2}{12}\left[\left(4\lambda_r^2 + 3\right)\left(\bar{\bar{\boldsymbol{\delta}}} - \mathbf{o}_r \mathbf{o}_r^T\right) + 6\mathbf{o}_r \mathbf{o}_r^T\right]$ is the inertia tensor of the element, expressed in the inertial frame of reference O; $\mathbf{o}_r$ and $\boldsymbol{\omega}_r$ are its orientation and angular velocity, respectively, while $\bar{\bar{\boldsymbol{\delta}}}$ is the identity matrix. The orientation vector evolves in time according to the equation: $\dot{\mathbf{o}}_r = \boldsymbol{\omega}_r \times \mathbf{o}$. The terms $\mathbf{T}_r^D$ and $\mathbf{H}_r^D$ represent the hydrodynamic viscous drag torque due to the relative spin between the fiber and the surrounding fluid, and the hydrodynamic drag torque due to the action of the fluid velocity gradients on the element, respectively. The contribution to the total torque of the constraint forces, $l_r \boldsymbol{o}_r \times (\mathbf{X}_{r+1} + \mathbf{X}_r)$, is also considered. In Eq. (5), vector $\mathbf{p}_r$ represents the position of the center of mass of the rth fiber element, which evolves in time according to the equation $\dot{\mathbf{p}}_r = \mathbf{v}_r$.

The system of Eqs. (3–5) is solved for each element of each fiber injected into the flow. The expressions used to compute the drag force and torques are selected based on the specific value of the element Reynolds number, defined as:

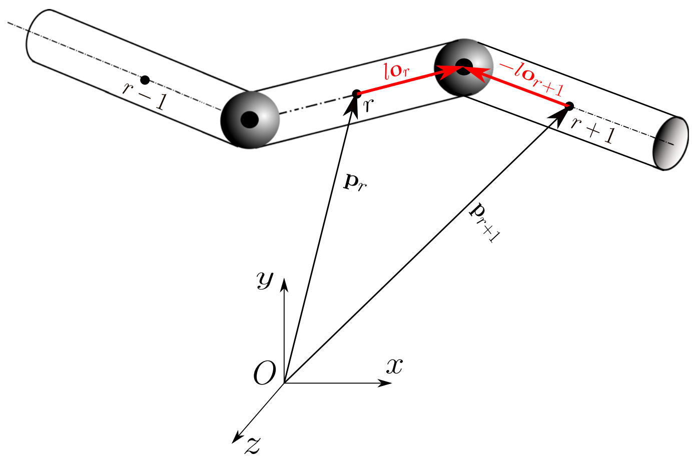

Fig. 2 Inextensibility kinematic constraint applied to the elements r and $r+1$ of the fiber

$$Re_{p,r} = \frac{2a}{\nu} \underbrace{\left| \left(\bar{\bar{\delta}} - \mathbf{o}_r \mathbf{o}_r^T \right) (\mathbf{u}_r - \mathbf{v}_r) \right|}_{v_{\perp,r}} . \tag{6}$$

The mathematical model and the expressions used for the hydrodynamic force and torques are given in Appendix 5.1, while the $\mathcal{LU}$ factorization used to solve the tridiagonal block matrix system associated with the constraint equation is given in Appendix 5.2.

Some features of the mechanics of the fibers have been neglected in the model. These include plastic deformations and effects due to fiber bending (no bending stiffness). Because we are interested in investigating fiber behavior in dilute flow conditions, fiber–fiber collisions have also been discarded. Collisions are also possible between elements belonging to the same fiber. However, it has been verified that such occurrence is extremely rare in the present flow configuration, and therefore, this type of collision was neglected. So were interactions between fiber elements due to lubrication, van der Waals and/or electrostatic forces. The strain of the fiber in the length direction was not included as well, since the deformation due to axial strain is small in comparison with those introduced by fiber bending for a wide range of fiber flexibilities, as shown by [28]. We believe that, as long as dilute flow conditions apply, all the above-mentioned simplifications may only provide minor quantitative changes to the statistical observables presented in Sect. 3.

2.3 Summary of simulations

Simulations are carried out at friction Reynolds number $Re_\tau = u_\tau h/\nu = 150$, where $u_\tau = 0.1177$ m/s is the friction velocity based on the mean wall shear stress and on fluid density, $\nu = 1.57 \cdot 10^{-5}$ m^2/s is fluid viscosity, and $h = 0.02$ m is the channel half height. The corresponding bulk Reynolds number is $Re = u_b h/\nu = 2250$, where $u_b = 1.77$ m/s is the bulk velocity. The Reynolds number based on the hydraulic diameter is $Re_D \simeq 9000$. The size of the computational domain is $1885 \times 942 \times 300$ wall units (i.e., in terms of variables identified with the superscript "+" made dimensionless using ν and u_τ) in x, y, and z, discretized with $128 \times 128 \times 129$ grid nodes. The non-dimensional step for time integration is 0.003 in wall units. The small time step size is imposed by numerical stability requirements (see [28] for a more detailed discussion).

Equations (1) and (2) are discretized using a pseudo-spectral method based on transforming the field variables into the wavenumber space, through a Fourier representation for the periodic (homogeneous) directions x and y and a Chebyshev representation for the wall-normal (non-homogeneous) direction z. A two-level explicit Adams–Bashforth scheme for the nonlinear terms and an implicit Crank–Nicolson method for the viscous terms are employed for the time advancement. As commonly done in pseudo-spectral methods, the convective nonlinear terms are first computed in the physical space and then transformed in the wavenumber space using a de-aliasing procedure based on the 2/3-rule; derivatives are evaluated directly in the wavenumber space to maintain spectral accuracy.

The evolution equation for the orientation vector $\mathbf{o}_r$ is integrated in time using a standard 4th-order Runge–Kutta scheme, while Eqs. (3)–(5) are solved using a mixed explicit/implicit differencing procedure developed by [18]. The same time step size as that of the fluid is used for integration, and the total Lagrangian tracking

Table 1 Summary of the simulation parameters relative to the fibers

St_r	St_f	λ_r	l_r^+	l_r (μm)	L_f^+	L_f/h	S
1	2.2	2	0.34	46.3	4.7	0.032	102.4
	1.8	5	0.85	116.0	11.75	0.079	66.5
5	11.0	2	0.34	46.3	4.7	0.032	512.0
	9.1	5	0.85	116.0	11.75	0.079	322.8
30	64.9	2	0.34	46.3	4.7	0.032	3071.8
	54.5	5	0.85	116.0	11.75	0.079	1996.5

The length of a fiber element is given both in wall units (l_r^+) and in dimensional units (l_r, microns). The length of the entire fiber is given in wall units (L_f^+) and as a function of the channel half height (L_f/h). Compared to Andric et al. [2], here we consider higher values of L_f/h (values in [2]: $0.013 < L_f/h < 0.03$) and similar density ratio, only the $St_r = 30$ fibers with $\lambda_r = 5$ (values in [2]: $1150 < S < 2300$)

time in wall units is $t^+ = t\nu/u_\tau^2 = 1250$, which was enough to reach the steady state in fiber wall-normal concentration. The relevant parameters for time integration are a, λ_r, and the response time of the fiber element [56]:

$$\tau_p = \frac{2a^2 S}{9\nu} \frac{\lambda_r \ln(\lambda_r + \sqrt{\lambda_r^2 - 1})}{\sqrt{\lambda_r^2 - 1}} . \tag{7}$$

The Stokes number of each fiber element is defined as $St_r = \tau_p/\tau_f$ with $\tau_f = \nu/u_\tau^2$. The different values of St_r considered in this study, together with the main simulation parameters characterizing the different fiber sets, are given in Table 1. The values of the Stokes number for the entire fiber in its fully stretched configuration, St_f (equivalent to the Stokes number of a rigid fiber with equal density and total length $L_f = 2 \cdot \mathcal{N} \cdot l_r$), and the values of the ratio between fiber density and fluid density, $S = \rho_p/\rho$, are also shown. We remark here that all fiber sets have the same dimensionless radius $a^+ \simeq 0.17$ corresponding to $a \simeq 11.8$ μm in dimensional units. To ensure converged statistics, swarms of $M = 10^5$ fibers, each having $\mathcal{N} = 7$ elements (as in [2]), are tracked for each combination of values in the (λ_r, St_r) space, assuming one-way coupling between the phases.

In the present flow configuration, the Kolmogorov length scale has a mean value $\eta^+_{K,\text{avg}} \simeq 2$ and varies from $\eta^+_{K,\text{min}} \simeq 1.62$ at the wall to $\eta^+_{K,\text{max}} \simeq 3.61$ at the channel center [46]. Therefore, individual fiber elements are smaller (or not longer, at least) than the smallest scale in the flow, but the entire fiber is longer regardless of λ_r. This implies that fiber elements will experience slightly different local flow conditions (velocity fluctuations and gradients) with respect to their neighbors [48]: Our model can take these differences into account and can reproduce their effect on the overall translational and rotational dynamics of the fiber. By doing so, we expect to observe a different long-term behavior in fiber dispersion compared to the case of rigid fibers, which evolve only according to the flow conditions at the position of the fiber center of mass.

3 Results and discussion

In this Section, we provide a statistical characterization of fiber translational and rotational dynamics inside the channel. Figure 3 provides a qualitative visualization of the instantaneous distribution of the $St_r = 5$ fibers in a fluid slab of size $698 < x^+ < 1306$, $297 < y^+ < 705$, $0 < z^+ < 150$. The non-homogeneous distribution attained by the fibers, which are released in a fully stretched configuration (all fiber elements are aligned) at random position and with random orientation, is evident and is biased by fiber inertia.
Our aim is to quantify the effect of flexibility on the macroscopic processes that stem from such distribution, namely preferential concentration and near-wall segregation [38]. To this aim, several statistical observables discussed in this Section provide direct comparison against the case of rigid fibers with equal shape and mass. Note that, in the present simulations, a rigid fiber is fully equivalent to a flexible fiber when the latter is completely stretched.

3.1 Fiber velocity statistics

The mean streamwise velocity, $\langle v_{x,G}\rangle$ (lines), of the different fiber sets is shown in Fig. 4, together with the mean streamwise velocity, $\langle u_{x,G}\rangle$ (symbols), of the fluid seen at the fiber's center of mass G. These profiles

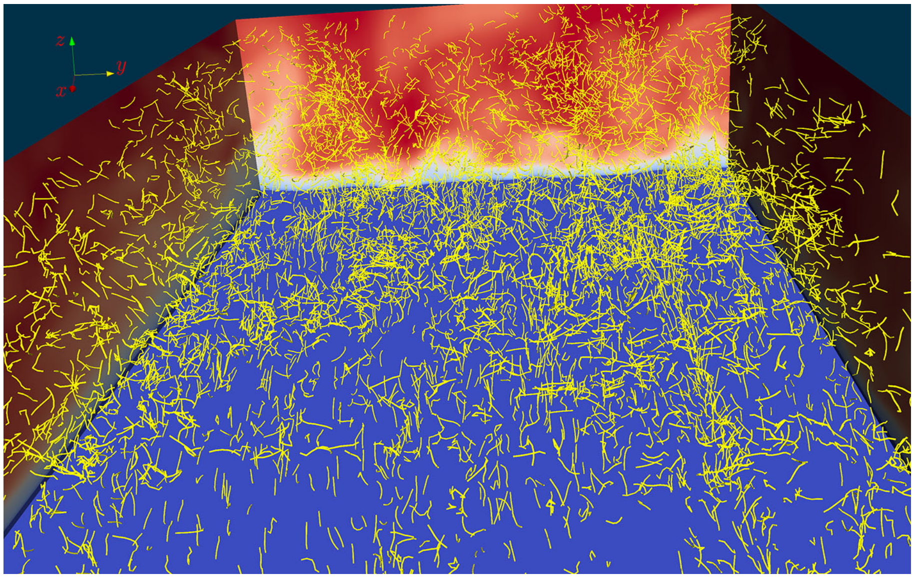

Fig. 3 Instantaneous distribution of $St_r = 5$ fibers in turbulent channel flow. For visualization purposes, only fibers in the slab $698 < x^+ < 1306$, $297 < y^+ < 705$, $0 < z^+ < 150$ are shown. Colormaps at the sides of the slab show the streamwise fluid velocity distribution (red: higher-than-mean velocity, blue: lower-than-mean velocity) (color figure online)

were obtained by computing the instantaneous values of v_x and u_x at the center of each fiber element (this implies interpolation for u_x) and then by averaging (i) over all elements of one fiber, (ii) over all fibers located at the same wall-normal distance, and (iii) over time: The resulting mean quantity is represented by angular brackets, $\langle \ldots \rangle$, hereinafter. Values for velocities are expressed in wall units, but the superscript + has been dropped for ease of notation. We remark that, different from a rigid fiber, the center of mass of a deformed fiber does not coincide with the center point of the fiber's middle element. Each panel in Fig. 4 refers to a different Stokes number and compares the velocity profiles for different aspect ratios. The horizontal axis starts at $z^+ = 1$ because the number of fibers comprised between the wall and this location is too low to ensure convergence of the statistics.

It is apparent that fibers with small inertia ($St_r = 1$, panel a) move at the same mean velocity of the surrounding fluid, lagging slightly the Eulerian fluid velocity in the buffer layer. As fiber inertia and elongation increase, $\langle v_{x,G} \rangle$ starts to deviate from $\langle u_{x,G} \rangle$, especially in the near-wall region where fibers appear to lead the fluid proportionally to their length. The extent of this region widens as the fiber Stokes number is increased, reaching out in the buffer region for the $St_r = 30$ fibers (Fig. 4c). Here, the tendency of fibers to lag behind the fluid and sample regions of the flow characterized by local fluid velocity lower than the mean is enhanced by inertia. These observations are in agreement with previous studies in which rigid fibers were considered [75], suggesting a negligible effect of deformability on the capability of fibers to maintain their streamwise momentum while drifting to the wall due to turbophoresis.

The difference between $\langle v_{x,G} \rangle$ and $\langle u_{x,G} \rangle$ indicates that a relative velocity between each fiber element and the local fluid is established. The resulting Reynolds number, $Re_{p,r}$, computed using Eq. (6), is shown in Fig. 5 as function of the wall-normal distance. Note that $Re_{p,r}$ depends not only on the relative velocity, but also on the orientation of the fiber element for which it is computed. In other words, different values of $Re_{p,r}$ can be obtained for fiber elements that have the same relative velocity with respect to the surrounding fluid but different orientation (or vice versa). The values attained by $Re_{p,r}$ determine the specific expression used to compute the drag coefficient $C_{D,r}$ according to Eq. (10). As expected, $Re_{p,r}$ increases as fibers approach the wall, and is larger for higher-inertia fibers. A maximum is reached around the location of maximum fiber-to-fluid relative velocity, but values remain always smaller than unity. Interestingly, $Re_{p,r}$ is larger for flexible fibers with lower aspect ratio (except for the $St_r = 30$ fibers inside a thin near-wall region). This is due to the fact that fibers with $\lambda_r = 2$ are characterized by higher density with respect to $\lambda_r = 5$ fibers (this is needed to keep the values of St_r and a^+ fixed) and, in turn, by higher mass and higher value of St_f; therefore, shorter fibers are expected to exhibit a larger relative velocity difference with respect to longer fibers in our simulations.

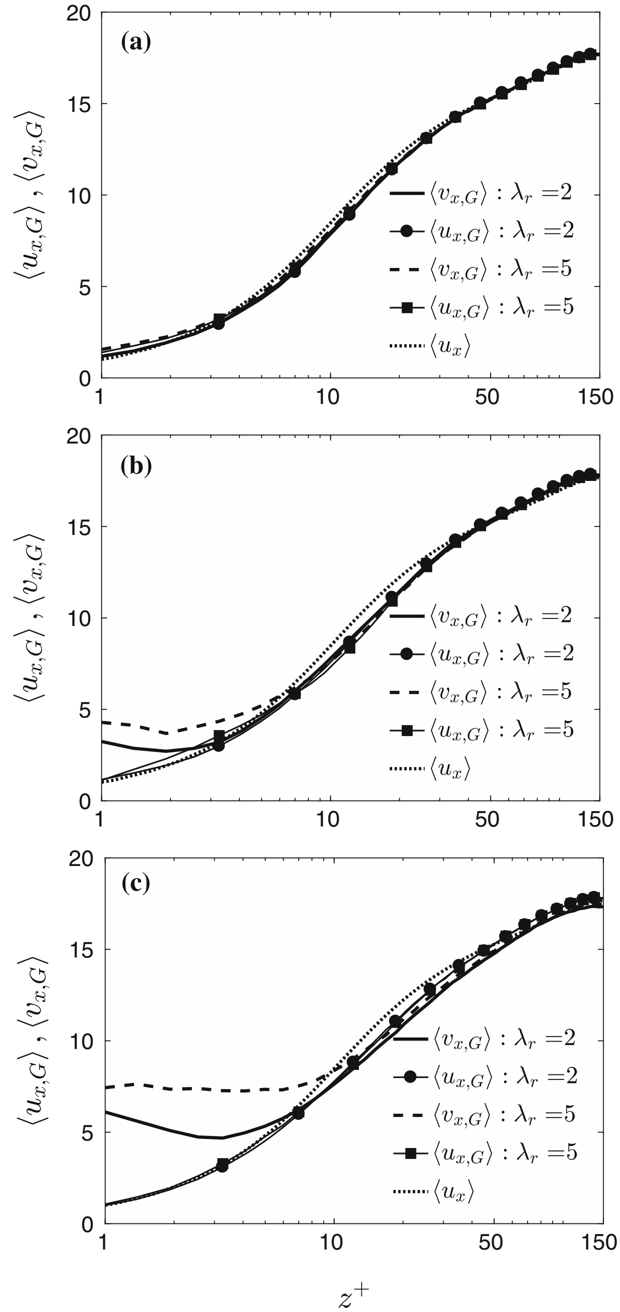

Fig. 4 Fiber mean streamwise velocity, $\langle v_{x,G}\rangle$. Subscript G indicates that the velocity at the fiber's center of mass G is considered. For comparison purposes, also the mean fluid velocity seen by the fibers is shown. **a** $St_r = 1$; **b** $St_r = 5$; **c** $St_r = 30$. Symbols represent fluid velocity interpolated at point G, solid and dashed lines represent fiber velocity, and dotted lines represent the Eulerian fluid velocity

In Fig. 6, we show the turbulent Reynolds stress of the fibers, $\langle v'_{x,G} v'_{z,G}\rangle$, for all the simulated sets. As in Fig. 4, the statistical observable for the fibers is compared with that of the fluid computed at the grid points of the Eulerian mesh, $\langle u'_x u'_z\rangle$ and with that of the fluid seen by each fiber along its trajectory, $\langle u'_{x,G} u'_{z,G}\rangle$. It can be seen that $\langle v'_{x,G} v'_{z,G}\rangle$ is only weakly affected by the aspect ratio at all Stokes numbers. For fibers with low inertia (Fig. 4a), preferential segregation effects are not strong enough to produce a bias between $\langle v'_{x,G} v'_{z,G}\rangle$ and $\langle u'_{x,G} u'_{z,G}\rangle$, which are both higher than the Eulerian stress $\langle u'_x u'_z\rangle$ in magnitude. At intermediate inertia (Fig. 4b), all curves overlap whereas a clear damping of the fiber stress is observed at high inertia (Fig. 4c).

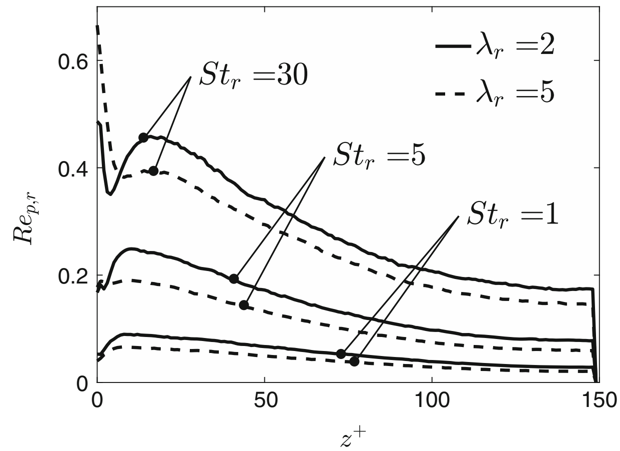

Fig. 5 Fiber element's mean Reynolds number, $Re_{p,r}$. Solid lines: $\lambda_r = 2$; dashed lines: $\lambda_r = 5$

In the latter case, the magnitude of $\langle v'_{x,G} v'_{z,G} \rangle$ is lower than both the Reynolds stress "seen" and the Eulerian Reynolds stress, regardless of the aspect ratio. The observed damping is purely an inertial effect.

Because fibers are anisotropic in shape, their rotational dynamics is also important to understand their interaction with the flow. In Fig. 7, we show the spanwise component of the mean angular velocity, $\langle \omega_{y,G} \rangle$, for the different fiber sets. This observable quantifies the ability of the fiber to perform tumbling-like rotations in the longitudinal x–z plane. The mean angular velocity of the fluid "seen," $\langle \Omega_{y,G} \rangle$ (computed at the fiber's center of mass), and the mean Eulerian angular fluid velocity, $\langle \Omega_y \rangle$ (computed considering only values of Ω_y at the computational grid points), are also shown. The streamwise and wall-normal components are not shown since their average value in the wall-normal direction is always equal to zero. Lines and symbols are as in Fig. 4. Different from the translational velocities, the fiber angular velocity (lines) exhibits significant deviations from that of the fluid "seen" (symbols) for all St_r: Fibers always lag the fluid and rotate at a slower rate, especially when characterized by small inertia. Note that the fibers sample fluid regions characterized by angular velocity larger than the Eulerian one. We also observe that the behavior of $\langle \omega_{y,G} \rangle$ is dependent on the aspect ratio (namely on the rotational inertia of the fiber), which has no effect on $\langle \Omega_{y,G} \rangle$: Shorter fibers tend to rotate faster than longer ones, this tendency being more evident for small fiber inertia. As discussed in [35], the rotational inertia of an elongated particle can be parameterized by a Stokes number $St_{\mathrm{rot},\perp}$, referred to the minor symmetry axes of the fiber, which quantifies the inertial response of the fiber to tumbling (rotation of the fiber around either of its minor axes), and a Stokes number $St_{\mathrm{rot},\parallel}$, referred to the major symmetry axis of the fiber, which quantifies the inertial response of the fiber to drilling (rotation of the fiber around its major axis). It can be shown that $St_{\mathrm{rot},\perp}$ increases with aspect ratio, whereas $St_{\mathrm{rot},\parallel}$ decreases. This implies that, in our simulation setting, fibers with higher aspect ratio exhibit higher rotational inertia with respect to tumbling and tend to tumble more than short fibers, thus explaining the trends shown in Fig. 7.

3.2 Fiber orientation statistics

The orientation of the fibers within the flow provides useful information about their preferential alignment. In Fig. 8, we show the probability density function (PDF) of the fiber mean orientation in the streamwise and wall-normal directions, indicated as $\langle o_x|_G \rangle$ and $\langle o_z|_G \rangle$, respectively. All fiber sets are considered, and PDFs are conditioned to the location of the fiber in the wall-normal direction: Thick lines refer to PDFs computed considering only fibers in a near-wall region of thickness equal to $5\delta_{\mathrm{VS}}$, with δ_{VS} the viscous sublayer thickness (equal to 6 wall units in the present simulations); symbols refer to PDFs computed considering only fibers in the bulk of the flow (namely fibers located at distances larger than $5\delta_{\mathrm{VS}}$ from the wall). The thin solid line in each panel represents the PDF corresponding to a random distribution of fiber orientations in a three-dimensional domain. We remind that the components o_x and o_z of the orientation vector are equal to the absolute value of the cosine of the angle between the major axis of the fiber element and the streamwise and wall-normal coordinates of the Cartesian frame of reference, respectively. Therefore, $o_j = 1$ means that the fiber is aligned with the jth flow direction and $o_j = 0$ means that the fiber is orthogonal to such direction. Because we are examining flexible fibers, an orientation can be computed for each element of the fiber. The profiles shown in

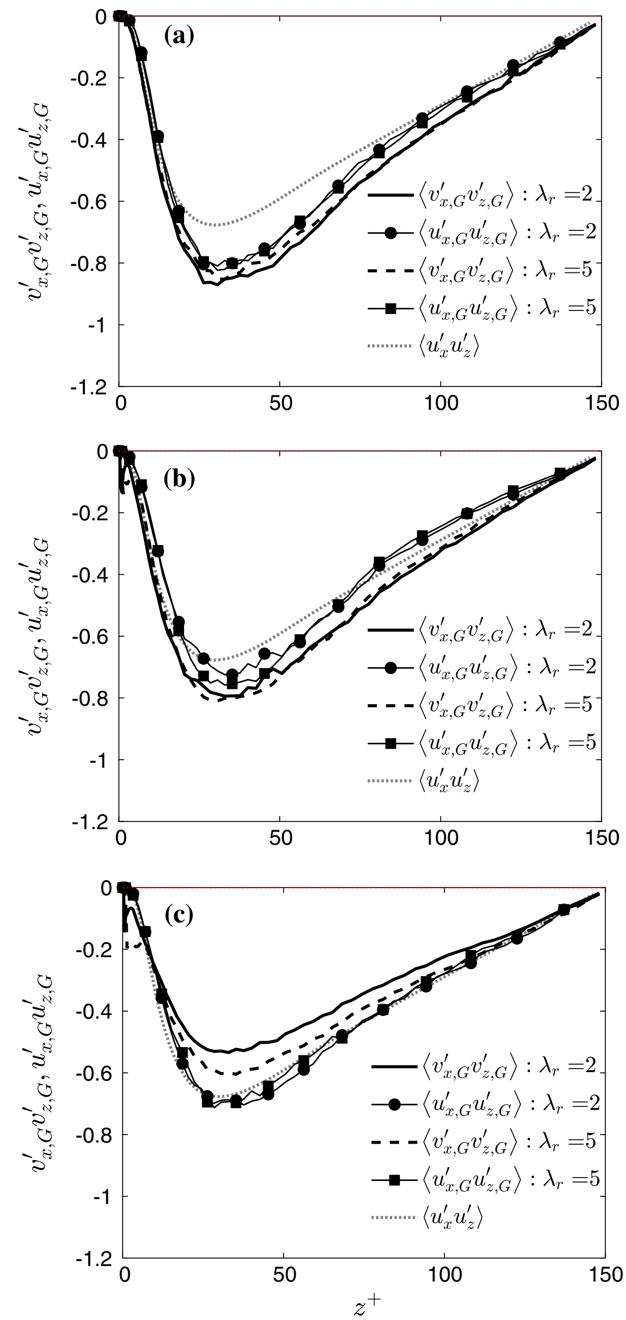

Fig. 6 Fiber Reynolds stress, $\langle v'_{x,G}v'_{z,G}\rangle$. For comparison purposes, also the Reynolds stress of the fluid seen by the fibers, $\langle u'_{x,G}u'_{z,G}\rangle$, is shown. **a** $St_r = 1$; **b** $St_r = 5$; **c** $St_r = 30$. Symbols represent the Reynolds stress of the fluid interpolated at point G, solid and dashed lines represent the Reynolds stress of the fiber, dotted lines represent the Eulerian fluid Reynolds stress, $\langle u'_x u'_z\rangle$

Fig. 8 were obtained upon averaging o_x and o_z over all elements of each flexible fiber and then averaging the resulting values over all fibers pertaining to the same near-wall or bulk-flow fluid slab.

For the case of fibers with low inertia ($St_r = 1$, panels (a) and (b) in Fig. 8), a significant difference can be observed between the near-wall PDF and the bulk-flow PDF for both aspect ratios examined. The near-wall PDF is negatively skewed for $\langle o_x|_G\rangle$ and positively skewed for $\langle o_z|_G\rangle$. This indicates that $St_r = 1$ fibers are preferentially aligned with the streamwise flow direction and perpendicular to mean shear. This trend is more evident for the longer fibers (compare dashed and solid lines). The bulk-flow PDF is more symmetric

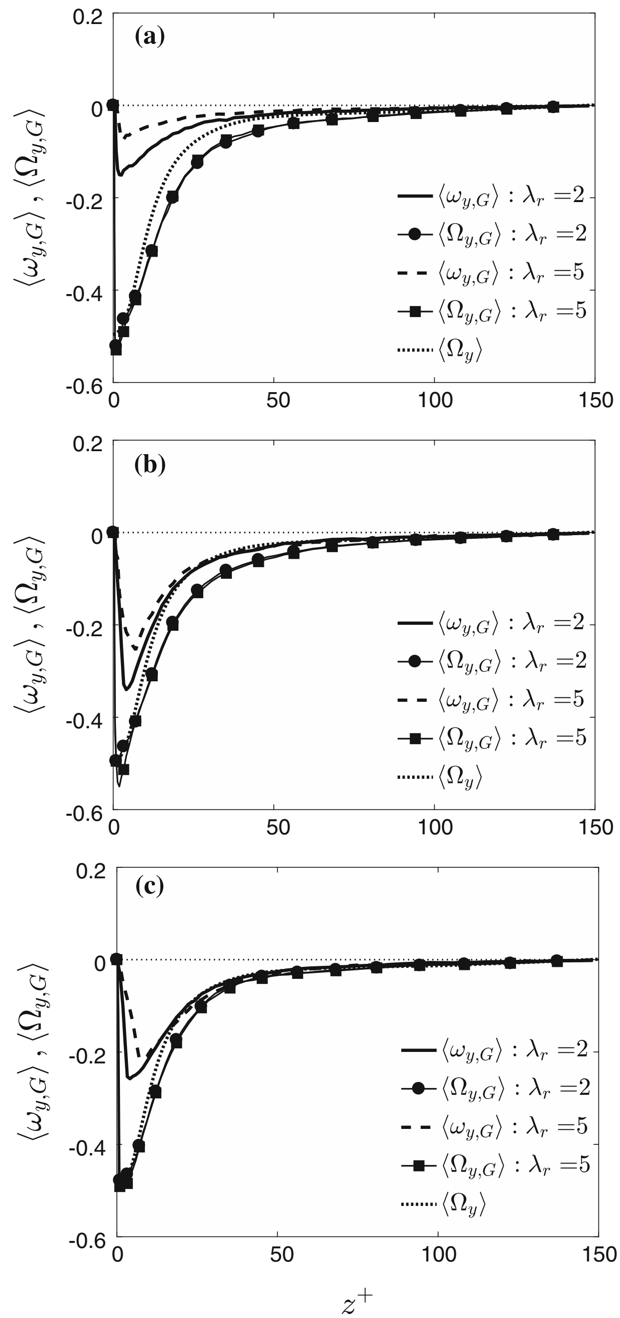

Fig. 7 Fiber mean spanwise angular velocity, $\langle\omega_{y,G}\rangle$. Subscript G indicates that only the velocity at the fiber's center of mass G is considered. **a** $St_r = 1$; **b** $St_r = 5$; **c** $St_r = 30$. Lines and symbols are as in Fig. 4

and relatively insensitive to the aspect ratio. This finding is in agreement with the fact that turbulence in the central region of the channel is more homogeneous and isotropic, and, hence, is expected to induce little or no preferential orientation. The symmetry of the bulk-flow PDF is maintained also at higher Stokes numbers, even if a non-negligible λ_r-dependence is observed. What is more interesting to discuss is the behavior of the near-wall PDF, which changes significantly between $St_r = 5$ and $St_r = 30$. At the intermediate Stokes numbers (panels (c) and (d) in Fig. 8), the PDFs of the $\lambda_r = 5$ fibers are just slightly skewed, indicating that the increase in fiber inertia has reduced the tendency to attain a preferential orientation within the flow. The PDF of $\langle o_x|_G\rangle$ for the $\lambda_r = 2$ fibers (panel (c) in Fig. 8), however, exhibits a sharp peak at values close to unity, which is associated with a marked drop in the PDF of $\langle o_z|_G\rangle$ (panel (d) in Fig. 8). This peak is due to fiber trapping in a thin region very close to the wall: In this region, alignment with the mean flow direction is

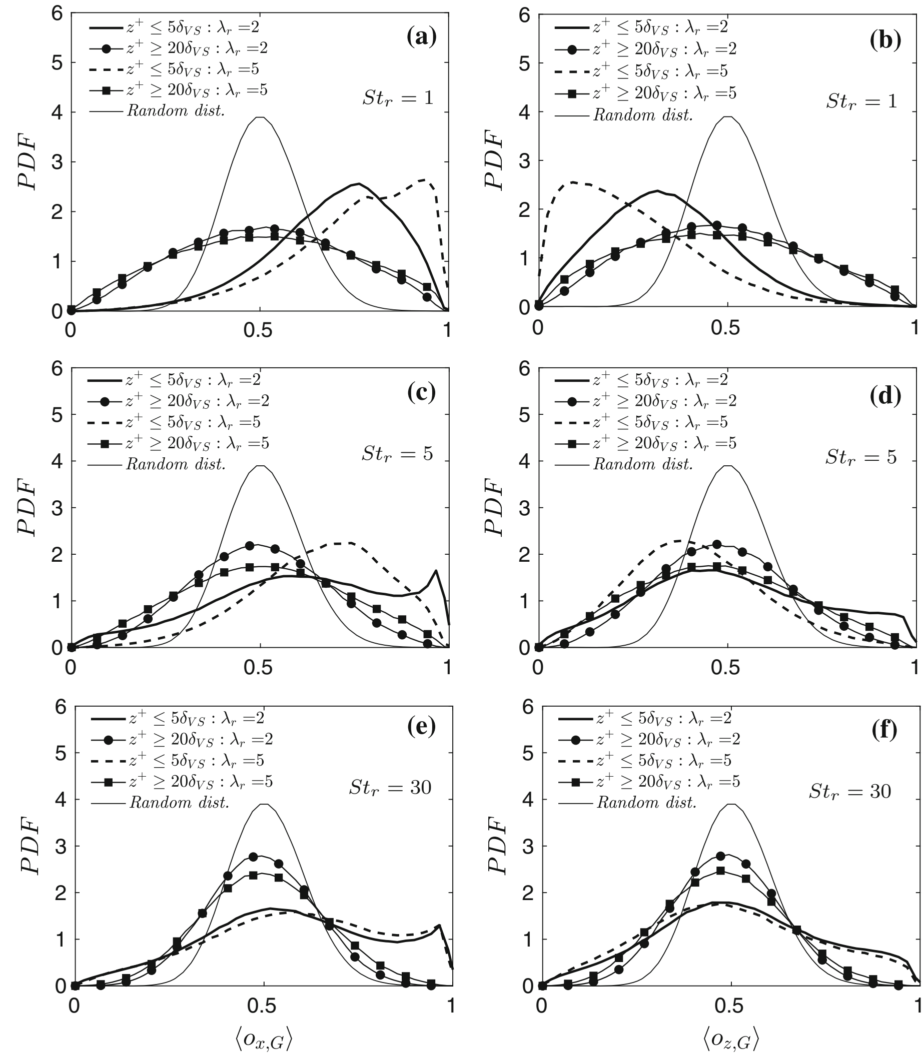

Fig. 8 Fiber mean orientation in the streamwise and wall-normal directions, $\langle o_x|_G \rangle$ and $\langle o_z|_G \rangle$, respectively. Subscript G indicates that the orientation of the fiber's center of mass is considered. **a**, **b** $St_r = 1$; **c**, **d** $St_r = 5$; **e**, **f** $St_r = 30$. Thick solid lines represent the orientation of fibers in a near-wall slab of thickness $0 \leq z < 5\delta_{\mathrm{VS}}$ with δ_{VS} the thickness of the viscous sublayer. Symbols represent the orientation of fibers in a core-flow slab of thickness $5\delta_{\mathrm{VS}} \leq z^+ \leq h$. The thin solid line in each panel represents the PDF corresponding to a random distribution of orientations in a three-dimensional domain

determined by the geometric constraint imposed by the presence of the wall in combination with the fiber–wall interaction model adopted in the present study. The striking difference between the PDFs occurring at $St_r = 5$ is lost almost completely at $St_r = 30$: In this latter case, fiber inertia is high enough to damp any effect due to the fiber aspect ratio in the near-wall region. More in general, fiber flexibility is seen to become of secondary importance when fiber inertia is large.

3.3 Fiber wall-normal concentration and near-wall segregation

Because of inertia, elongation, and flexibility, the macroscopic outcome of fiber translational and orientational behavior is twofold: A non-homogeneous spatial distribution is attained in both the wall-normal and wall-parallel directions. To characterize statistically such distributions, we focus here on two observables: the fiber particle number density, referred to as concentration hereinafter (shown in Fig. 9), and the PDF of the fluid velocity fluctuations sampled by the fibers in the near-wall region (shown in Fig. 11).

Fiber concentration, $C_G/C_{0,G}$, is computed as follows: (i) The flow domain is divided into N_s wall-parallel fluid slabs of equal thickness; (ii) the number $N_{f;s}(t)$ of fibers with center of mass G falling in each fluid slab at a

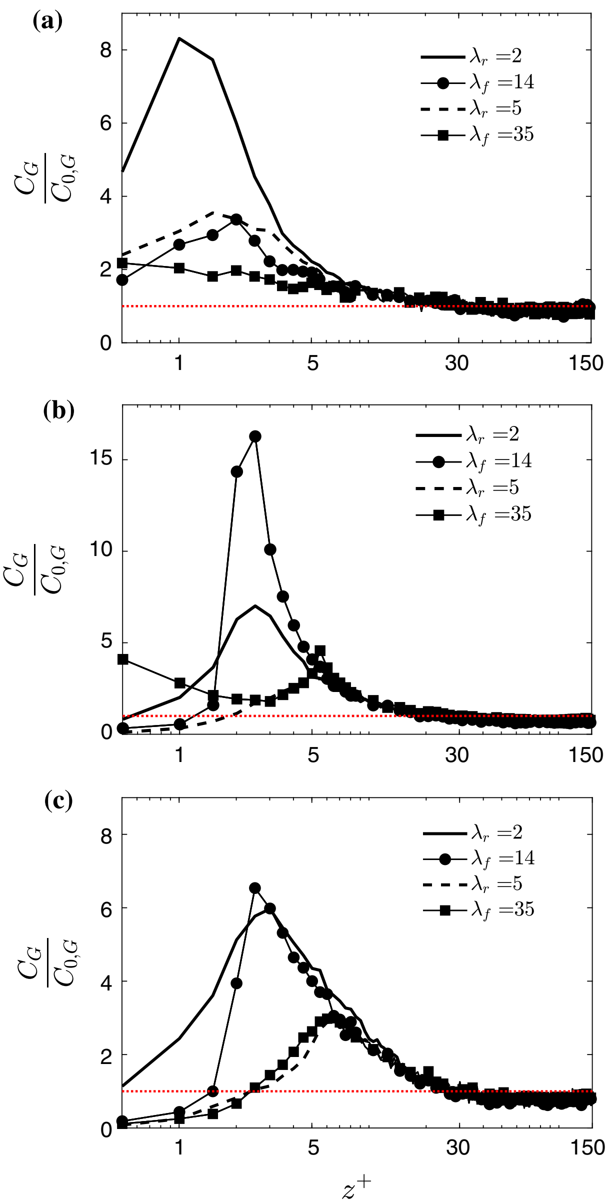

Fig. 9 Instantaneous fiber concentration (number density distribution) along the wall-normal direction. Profiles are taken at time $t^+ = 1250$. **a** $St_r = 1$; **b** $St_r = 5$; **c** $St_r = 30$

given time step is counted; (ii) the number density $C_G(t) = N_{f;s}(t)/V_s$ is computed, with V_s the volume of the sth slab; (iv) the normalized concentration is obtained dividing $C_G(t)$ by its initial value $C_{0;G} = C_G(t = 0)$. By doing so, values of $C_G/C_{0;G}$ larger (resp. smaller) than unity indicate accumulation (resp. depletion) of fibers. Profiles shown in Fig. 9 refer to time $t^+ = 1250$ of the simulations and were obtained using $N_s = 150$. To highlight the effect of flexibility on wall-normal accumulation, profiles for flexible fibers (lines in Fig. 9) are contrasted with profiles for "equivalent" rigid fibers having the same physical and geometrical parameters (symbols in Fig. 9). At low fiber inertia (Fig. 9a), the concentration of flexible fibers in the near-wall region is always higher than that of rigid fibers, indicating that flexible fibers experience a stronger wallward turbophoretic drift. This allows a more efficient trapping of the flexible fibers inside the viscous sublayer, in particular within 2 or 3 viscous units from the wall. At intermediate inertia (Fig. 9b), the largest differences are observed for the shorter $St_r = 5$ fibers: In this case, the peak of concentration for flexible fibers (solid line), located at $z^+ \simeq 2.5$, is significantly lower than that of the rigid fibers (circles), but the number of flexible fibers in the last 1.5 viscous units from the wall is higher. The concentration profile for the longer $St_r = 5$

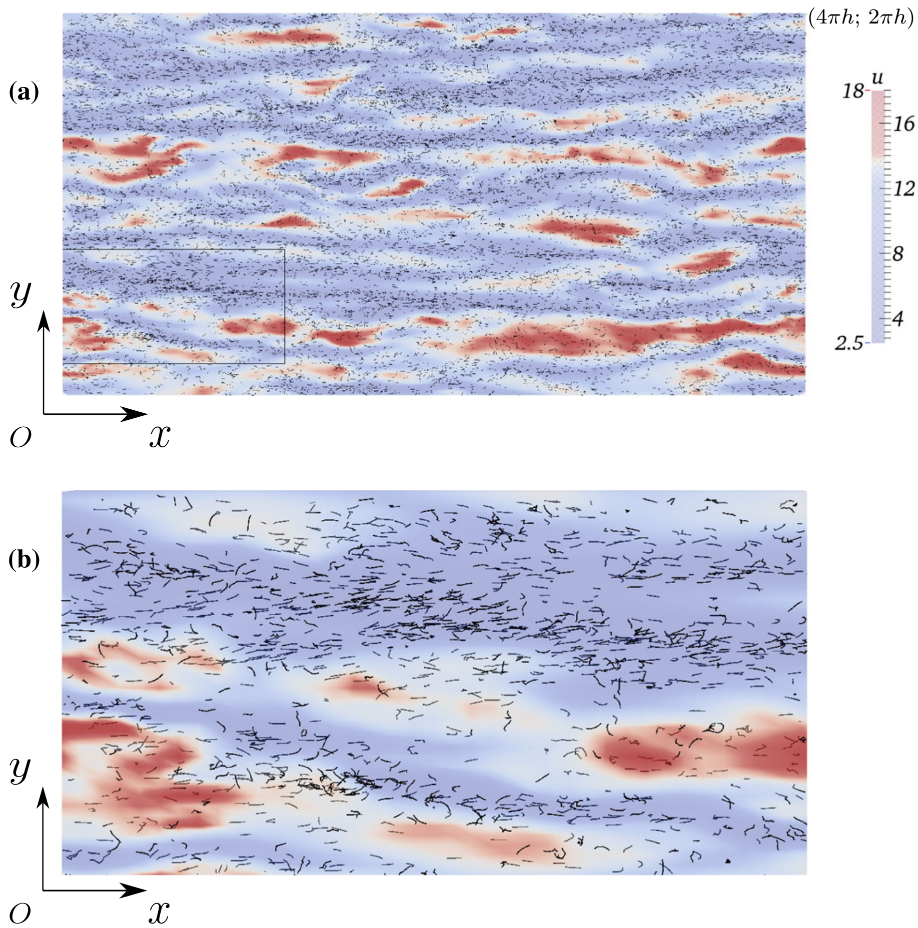

Fig. 10 Instantaneous fiber distribution in the near-wall region. For visualization purposes, only the $St_r = 5$ fibers with $\lambda_r = 5$ in the slab $0 < z^+ < 30$ are shown. The colormap shows the streamwise fluid velocity fluctuations (red: high-speed streaks with $u'_{G,x} > 0$, blue: low-speed streaks with $u'_{G,x} < 0$). **b** is a close-up view of the rectangular region highlighted in **a** (color figure online)

fibers (dashed line) does not differ much from that of the rigid fibers (squares), even if a slightly lower peak of concentration is observed for the flexible fibers. Examining now the $St_r = 30$ fibers (Fig. 9c), we observe again that flexibility is associated with stronger accumulation in close proximity to the wall, especially in the $\lambda_r = 2$ case. In this case, it can also be noted that the peak value of concentration is not much affected by the increase in inertia (this value being nearly the same as that obtained for the $St_r = 5$ fibers), whereas a strong decrease is found for the rigid fibers (from $C_G/C_{0;G} \simeq 16$ in panel b to $C_G/C_{0;G} \simeq 6$ in panel c). Overall, rigid fibers seem to be more sensitive to a change in their inertia as far as wall-normal accumulation is concerned, and flexibility appears to produce significant quantitative modifications to concentration profiles.

The analysis of concentration profiles indicates that, in agreement with the findings of previous studies on pointwise spherical particles (see [58] for a review) and rigid fibers [37], wall accumulation of flexible fibers is driven by turbophoresis and modulated by fiber inertia. In view of this analogy, it is therefore natural to expect similarities in the spatial distribution of the trapped fibers, namely formation of elongated streaks within the low-speed regions of the flow. A sample snapshot of the instantaneous distribution of the flexible fibers in the present simulation setting is provided in Fig. 10. The $St_r = 5$ fibers with $\lambda_r = 5$ are chosen as reference for visualizations. The correlation between fiber clusters and low-speed regions (in blue) is quite clear and can be appreciated better in the close-up view of Fig. 10b, where high-speed regions (in red) appear depleted of particles. To quantify this correlation, in Fig. 11 we show the PDF of the streamwise fluid velocity fluctuations, $\langle u'_{x,G} \rangle$, sampled at the position of the fiber's center of mass G. The PDF is conditioned to the wall-normal location of G: Only fibers with center of mass within a near-wall region of thickness $\Delta z^+ = 30$, considered as trapped, were taken into account for the calculation. For comparison purposes, the PDFs for flexible fibers

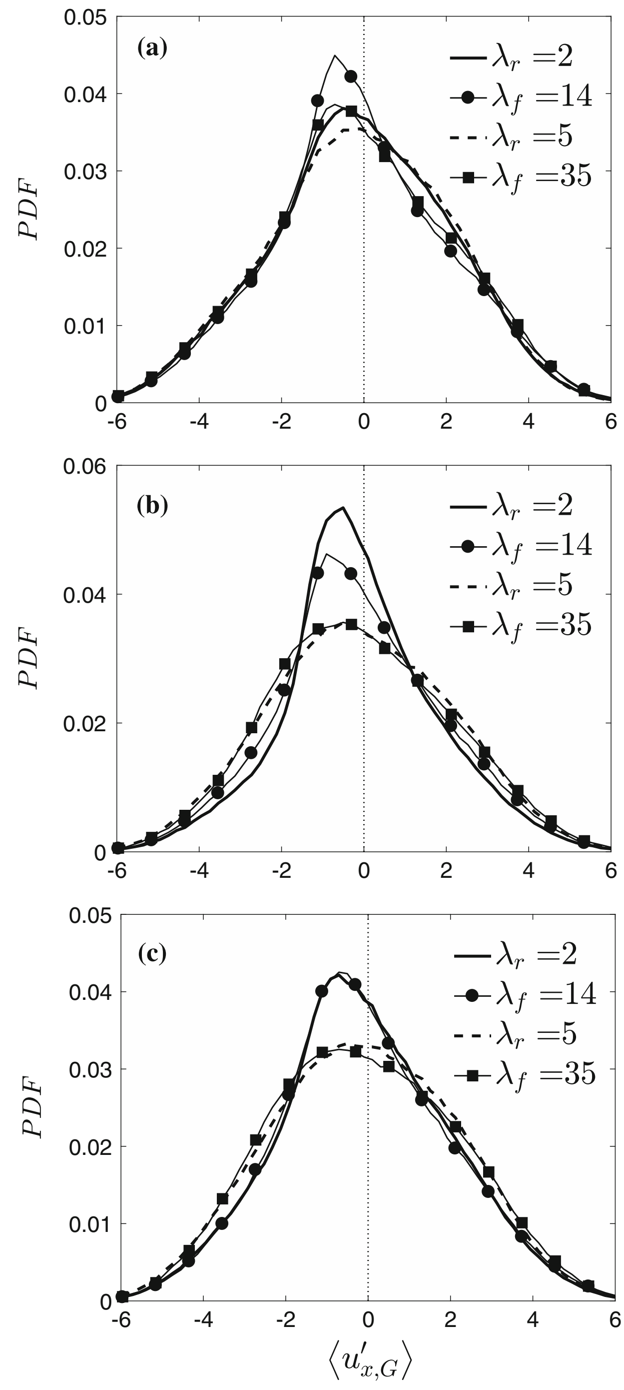

Fig. 11 PDF of the fluid velocity fluctuations sampled at the position of the fiber's center of mass G in the near-wall region (in a fluid slab $\Delta z^+ = 30$ thick). **a** $St_r = 1$; **b** $St_r = 5$; **c** $St_r = 30$

(lines) are shown together with the PDFs for rigid fibers with the same physical and geometrical parameters (symbols). As previously, angular brackets denote triple averaging: over all elements of a single fiber, over all fibers in the selected fluid slab, and over time. Comparing the three panels of Fig. 11, the following observations can be made. First, the effect of flexibility on segregation into low-speed streaks is limited to fibers with low or intermediate inertia: In the $St_r = 1$ case, the peak of the PDF for both the $\lambda_r = 2$ fibers and the $\lambda_r = 5$ fibers in the negative $\langle u'_{x,G} \rangle$ semi-plane decreases with respect to the rigid fibers, and the curve is more negatively skewed in the positive $\langle u'_{x,G} \rangle$ semi-plane, indicating weaker segregation; in the $St_r = 5$ case, the peak of the

PDF for the $\lambda_r = 2$ fibers in the negative $\langle u'_{x,G} \rangle$ semi-plane increases, and the curve is less negatively skewed in the positive $\langle u'_{x,G} \rangle$ semi-plane, indicating stronger segregation. In all other cases, namely $St_r = 5$ fibers with $\lambda_r = 5$ and $St_r = 30$ fibers (regardless of the aspect ratio), the deviation of the PDFs is minor indicating no effect on segregation. In particular, as the Stokes number is increased, inertia appears to dominate over flexibility even if changes in the shape of the PDF due to the different fiber elongation become more evident: Longer fibers, no matter if rigid or flexible, exhibit stronger tendency to segregate in low-speed streaks, in agreement with the findings of [37].

The statistical observables discussed in this Section demonstrate that flexibility can lead to significant quantitative changes in the macroscopic phenomena associated with inertia-driven preferential concentration and that the importance of these changes on fiber dynamics depends in a non-trivial way on the aspect ratio.

3.4 Fiber bending

One last aspect of fiber dynamics that we wish to investigate in this paper is bending, induced by the fluid velocity gradients acting along the fiber. Even if our study is based on a point-particle approach, the model used to approximate the fiber can take into account the effect due to a spatial change in such gradients by considering their value at the center of each element composing the fiber. To quantify bending, we use the three-dimensional fiber end-to-end distance, shown in Fig. 12, as a function of the wall-normal coordinate, in dimensionless form (wall units) and for all fiber sets. Profiles refer to a mean distance, averaged over all fibers in the flow domain and in time (over the last 90 viscous time units of the simulation). The length of a fully stretched fiber, represented by the horizontal thin lines in Fig. 12, is $L_f^+ = 4.7$ for fibers with $\lambda_r = 2$ and $L_f^+ = 11.75$ for fibers with $\lambda_r = 5$: Lower values of L^+ indicate bending. Starting from the wall and moving away from it, we observe an increase in L^+ for all fiber sets. In the $St_r = 1$ case (Fig. 12a), this increase continues up to $z^+ \simeq 20$: Beyond this point, the curves reach a plateau that is maintained throughout the core region of the flow. The plateau value of L^+ is roughly equal to $0.6L_f^+$ regardless of the element's aspect ratio. In the $St_r = 5$ case (Fig. 12b), L^+ reaches a rather sharp maximum at $z^+ \simeq 10$–15, indicating local stretching, and then drops to a uniform value (again approximately equal to $0.6L_f^+$) beyond $z^+ \simeq 50$ from the wall. In the $St_r = 30$ case (Fig. 12c), the maximum of L^+ is more evident and corresponds to a wider region of fiber stretching. As before, we find that the ratio of the end-to-end distance to the length of the fully stretched fiber is roughly equal to 0.6. This result is in agreement with the finding that the average solid angle (given by the relative orientation of two neighboring fiber elements in 3D space) measured outside of the buffer layer is characterized by a rather symmetric PDF (not shown), with a peak at $\langle \alpha \rangle \simeq 60°$ for all simulated sets. It also suggests that fiber bending away from the wall is weakly dependent on St_r and λ_r. This independency can be attributed to the fact that, outside of the buffer layer, the length of one fiber element is significantly smaller than the local Kolmogorov scale, and the length of the entire fiber is smaller than $7\eta_k$, a value for which fiber rotation is independent of inertia [44]. Finally, we remark that the region of largest stretching correlates well with the region of maximum turbulent Reynolds stress (see also Fig. 6) and that the strength of this correlation depends on inertia, as well as on elongation since longer fibers appear to get stretched closer to the wall than shorter ones.

Another observable that can be examined to characterize bending is the solid angle α between two neighboring fiber elements: $\alpha = 0$ corresponds to a fully stretched fiber in which all elements have the same orientation, whereas bending is associated with $\alpha > 0$. (The stronger the bending, the higher the value of α.) In Fig. 13, we show the scatter plot correlation between α (expressed in radiants) and the relative end-to-end distance, $L_f^+ - L^+$ (expressed in wall units). Since L_f^+ represents the maximum value that can be attained by the end-to-end distance, the limit cases are $L_f^+ - L^+ = 0$, when the fiber is completely stretched, and $L_f^+ - L^+ = L_f^+$ when the two ends of a fiber touch each other. The thick solid line in each panel represents the mean value of $L_f^+ - L^+$, obtained upon ensemble averaging over all points in the scatter plot and over time (essentially to get $\langle L^+ \rangle$). Error bars represent the standard deviation from such mean value and provide a measure of the uncertainty associated with the plots. It can be noted that there is a direct proportionality between α and $L_f^+ - L^+$: Stretched (resp. bent) fibers are characterized by large (resp. small) values of both α and $L_f^+ - L^+$, even if the distribution in the values of α at small end-to-end distance is rather widespread. In our view, this suggests that the information about fiber bending that could be obtained from the examination of the mean solid angle would not add to the findings already provided in Fig. 12. However, an analysis of

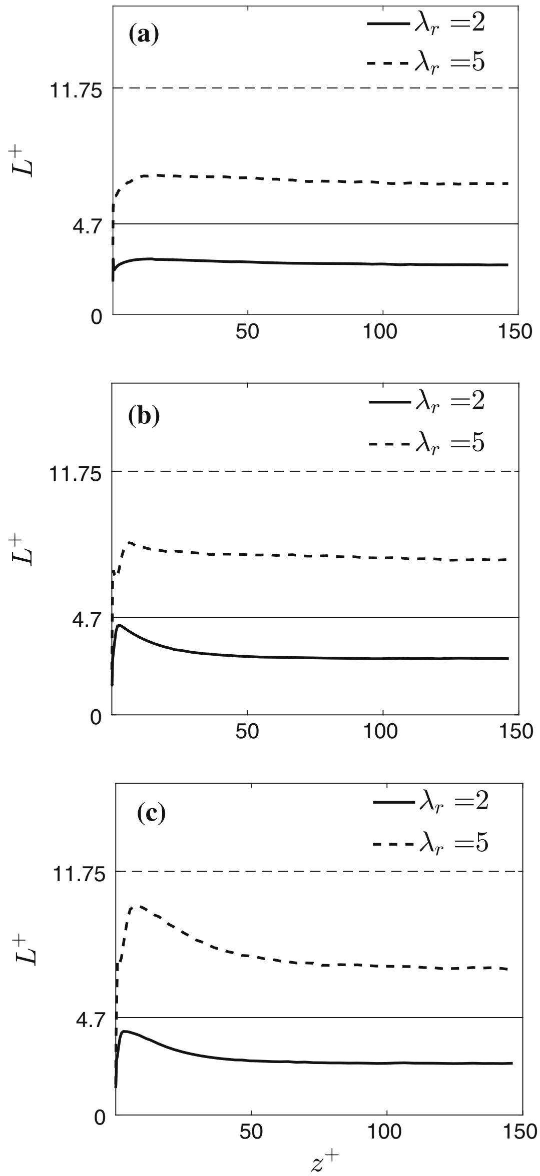

Fig. 12 Dimensionless fiber end-to-end distance, L^+. Panels: **a** $St_r = 1$; **b** $St_r = 5$; **c** $St_r = 30$

α could lead to interesting findings about the importance of the bending stiffness (which was not included in the present simulations). From Fig. 12, we see that, in the near-wall region, the most natural (or statistically probable) state for fibers with high inertia fibers is the stretched one, which corresponds to low values of $\langle\alpha\rangle$: In this case, bending stiffness would not play a very important role in fiber dynamics. On the other hand, we find significant near-wall deformation for fibers with low inertia, corresponding to high values of $\langle\alpha\rangle$: If the bending stiffness of these fibers would be accounted for, then they would drain a non-negligible amount of energy from the fluid, hinting to possible important two-way coupling effects (which we are currently investigating). The same would apply to fibers in the center of the channel, regardless of their inertia.

4 Conclusions and future developments

In this work, the dynamics of flexible fibers dispersed in a turbulent channel flow was examined using DNS and Lagrangian fiber tracking. The rod-chain model of Lindström and Uesaka [28] was chosen because it reproduces quite reasonably the behavior of flexible elongated fibers in unsteady flow. Results obtained for

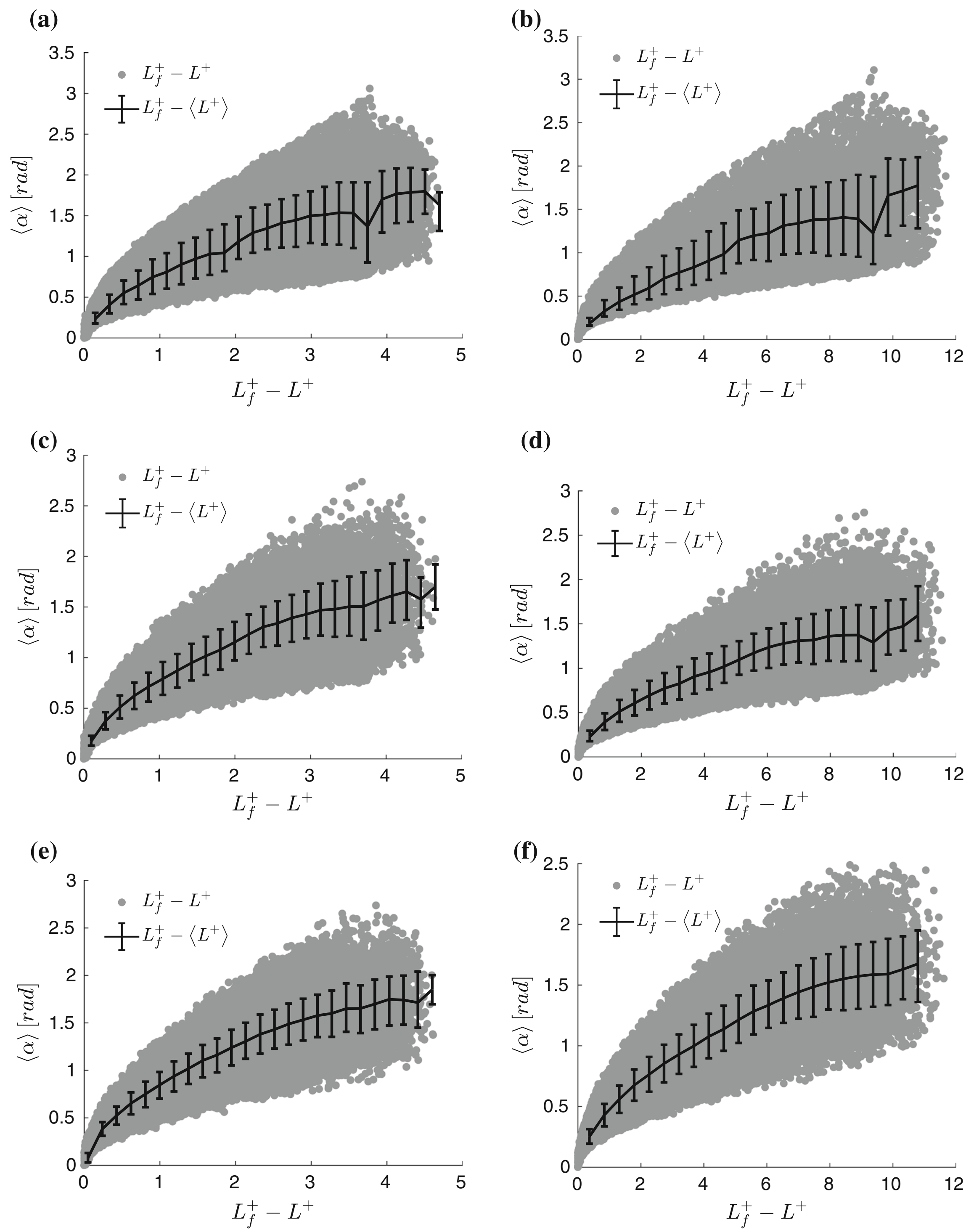

Fig. 13 Scatter plot of the correlation between the fiber end-to-end distance, $L_f^+ - L^+$, and the mean solid angle between adjacent fiber elements, $\langle \alpha \rangle$. The solid line represents the mean value of the correlation. Error bars represent the standard deviation from the mean. Rows: **a**, **b** $St_r = 1$; **c**, **d** $St_r = 5$; **e**, **f** $St_r = 30$. Columns: **a**, **c**, **e** $\lambda_r = 2$; **b**, **d**, **f** $\lambda_r = 5$

different values sampling the (λ_r, St_r) space clearly indicate that the coupling between fiber translation and fiber rotation changes significantly their wallward flux with respect to rigid fibers with the same geometrical and physical parameters. This effect adds to that due to their elongated shape and to their inertia leading to a quantitative different buildup of fibers at the wall. In turn, this leads to stronger accumulation in the very-near-wall region, where flexible fibers appear to be trapped, segregated, and preferentially oriented by the same physical mechanisms (turbophoresis) that govern preferential concentration of spherical particles and rigid fibers in bounded flows. In the buffer layer and in the viscous sublayer, bending of flexible fibers with small inertia is enhanced by mean shear and turbulent Reynolds stresses, while being reduced for fibers with large inertia.

Future developments of this work are planned for both dilute and semi-dilute suspensions. In the dilute suspension limit, interesting aspects to be investigated are the effect of bending stiffness on the fiber deformation dynamics, the dependence of fiber deformation on the flow Reynolds number, and the impact of spatial filtering on fiber motion. In particular, the inclusion of an internal resistance torque in the rod-chain model equations will allow a more realistic representation of fiber bending dynamics and hopefully provide information about the formation of fiber flocs or hang-ups in regions of fiber preferential concentration. Fiber bending is ultimately determined by the hydrodynamic fluid–fiber interaction, and therefore, a dependency on the flow Reynolds number should be expected, in particular at Reynolds numbers significantly higher than $Re_\tau = 150$, for which turbulence intensity increases and local gradients become more intermittent. To simulate high-Re_τ flows, the DNS-based approach adopted in this study might become computationally unfeasible, and calculations based on large-eddy simulation of turbulence could be preferred. In this case, however, fibers would evolve in a spatially filtered flow field (especially on coarse grids) and would not be exposed to the action of the sub-grid fluid velocity fluctuations, which are known to affect the tendency of inertial particles to concentrate preferentially [34]. Investigations are underway to examine the effect of filtering on the motion of the flexible fibers and to assess the conditions (e.g., grid coarseness) under which a closure model is needed in the equation of fiber motion.

In the semi-dilute regime, we are currently running simulations at higher volume and mass fraction in order to evaluate the modulation of turbulence (and, in turn, on fiber motion) when two-way coupling between carrier phase and dispersed phase is taken into account. For elongated particles, in particular, both inter-phase momentum and and angular momentum exchange should be taken into account in view of the strong coupling between translation and rotation [1]. Two-way coupled simulations are expected to provide physical insight on the mechanism of turbulent drag reduction/increase, which has been observed in many experiments for different drag-reducing agents [17].

5 Appendices

5.1 Hydrodynamic force and torques

If $Re_{p,r} = 0$ (e.g., at the beginning of the tracking), then the analytical solution valid for Stokes flow conditions is adopted; if $Re_{p,r} > 0$, then inertial effects are incorporated via a suitably defined drag coefficient $C_{D,r}$. When Stokes flow condition applies, the analytical solution derived by Kim and Karrila [25] for the viscous drag force and torque generated on an isolated axisymmetric ellipsoid is extended to the present rod-like fiber elements using the semiempirical formula proposed by Cox [11]. This formula expresses the hydrodynamic similarity existing in shear flow between the orbiting behavior of a rod and that of a prolate spheroid with minor axis a_{el}, major semi-axis l_{el}, and aspect ratio λ_{el} (see Fig. 14):

$$\frac{\lambda_{el}}{\lambda_r} = \frac{1.24}{\sqrt{\ln(\lambda_r)}} \quad \Longleftrightarrow \quad a_{el} = \frac{a}{1.24}\sqrt{\ln(\lambda_r)}. \tag{8}$$

Even if Cox's formula is valid for an isolated slender particle, numerical experiments [28] have shown that the maximum error in model predictions of the orbit period for rigid fibers in shear flow is below 3% for the range of aspect ratios considered in the present study.

The drag force is $\mathbf{F}_r^D = \bar{\bar{\mathbf{A}}}_r^D(\mathbf{u}_r - \mathbf{v}_r)$, where $\mathbf{u}_r$ is the fluid velocity evaluated at the center of mass of the fiber element and $\bar{\bar{\mathbf{A}}}_r^D$ is the resistance drag force tensor defined as [25]:

$$\bar{\bar{\mathbf{A}}}_r^D = \begin{cases} 6\pi\lambda_r a\mu\left[X_r^A\bar{\bar{\boldsymbol{\delta}}} + \left(Y_r^A - X_r^A\right)\mathbf{o}_r\mathbf{o}_r^T\right] & \text{if } Re_{p,r} = 0; \\ 2C_{D,r}\rho\lambda_r a^2 v_{\perp,r}\left(\bar{\bar{\boldsymbol{\delta}}} - \mathbf{o}_r\mathbf{o}_r^T\right) & \text{if } Re_{p,r} > 0. \end{cases} \tag{9}$$

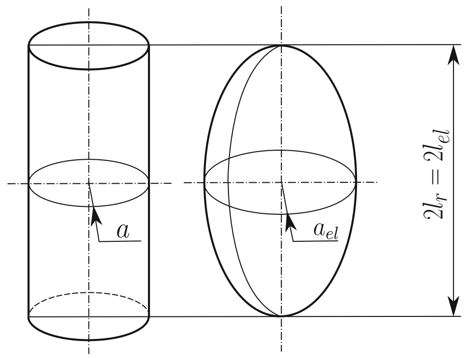

Fig. 14 Hydrodynamic equivalence for $Re_{p,r} = 0$ between a rod and an ellipsoidal particle via Cox's empirical formula [11]

The coefficients X_r^A and Y_r^A are defined as:

$$\begin{cases} X_r^A = \dfrac{8e_{c,r}^3}{-6e_{c,r} + 3\left(1 + e_{c,r}^2\right)\ln\left(\dfrac{1 + e_{c,r}}{1 - e_{c,r}}\right)}; \\ Y_r^A = \dfrac{16e_{c,r}^3}{6e_{c,r} + 3\left(3e_{c,r}^2 - 1\right)\ln\left(\dfrac{1 + e_{c,r}}{1 - e_{c,r}}\right)} \end{cases} \tag{10}$$

where $e_{c,r} = \sqrt{\frac{\lambda_r^2 a^2 - a_{el}^2}{\lambda_r^2 a^2}}$. The drag coefficient $C_{D,r}$ is computed using the following expressions [10]:

$$C_{D,r} = \begin{cases} C_{D,r}^I = 9.689 Re_{p,r}^{-0.78} & \text{if } Re_{p,r} \in \left]0, 0.1\right]; \\ C_{D,r}^I \left(1 + 0.147 Re_{p,r}^{0.82}\right) & \text{if } Re_{p,r} \in \left]0.1, 5\right]; \\ C_{D,r}^I \left(1 + 0.227 Re_{p,r}^{0.55}\right) & \text{if } Re_{p,r} \in \left]5, 40\right]; \\ C_{D,r}^I \left(1 + 0.0838 Re_{p}^{0.82}\right) & \text{if } Re_{p,r} \in \left]40, 400\right]; \\ 1 & \text{if } Re_{p,r} > 400. \end{cases} \tag{11}$$

The hydrodynamic drag torque is computed as $\mathbf{T}_r^D = \bar{\bar{\mathbf{C}}}_r^D \left(\boldsymbol{\Omega}_r - \boldsymbol{\omega}_r\right)$, where $\bar{\bar{\mathbf{C}}}_r^D$ is the resistance torque tensor, defined as [25]:

$$\bar{\bar{\mathbf{C}}}_r^D = \begin{cases} 8\pi \lambda_r^3 a^3 \mu \left[X_r^C \bar{\bar{\boldsymbol{\delta}}} + \left(Y_r^C - X_r^C\right) \mathbf{o}_r \mathbf{o}_r^T\right] & \text{if } Re_{p,r} = 0; \\ \frac{2}{3} C_{D,r} \rho \lambda_r^3 a^4 v_{\perp,r} \left(\bar{\bar{\boldsymbol{\delta}}} - \mathbf{o}_r \mathbf{o}_r^T\right) & \text{if } Re_{p,r} > 0 \end{cases} \tag{12}$$

where the coefficients X_r^C and Y_r^C are defined as [25]:

$$\begin{cases} X_r^C = \dfrac{4e_{c,r}^3\left(1 - e_{c,r}^2\right)}{6e_{c,r} - 3\left(1 - e_{c,r}^2\right)\ln\left(\dfrac{1 + e_{c,r}}{1 - e_{c,r}}\right)}; \\ Y_r^C = \dfrac{4e_{c,r}^3\left(2 - e_{c,r}^2\right)}{-6e_{c,r} - 3\left(1 + e_{c,r}^2\right)\ln\left(\dfrac{1 + e_{c,r}}{1 - e_{c,r}}\right)}. \end{cases} \tag{13}$$

The drag torque due to the velocity gradients at the position of the element's center of mass is defined as:

$$\bar{\bar{\mathbf{H}}}_r^D = \begin{cases} -8\pi \mu a^3 \lambda_r^3 Y_r^H \left(\bar{\bar{\boldsymbol{\varepsilon}}} \mathbf{o}_r\right) : \left(\dot{\bar{\bar{\boldsymbol{\gamma}}}}_r \mathbf{o}_r\right) & \text{if } Re_{p,r} = 0; \\ -\frac{2}{3} a^4 \lambda_r^3 C_{D,r} \rho v_{\perp,r} \left(\bar{\bar{\boldsymbol{\varepsilon}}} \mathbf{o}_r\right) : \left(\dot{\bar{\bar{\boldsymbol{\gamma}}}}_r \mathbf{o}_r\right) & \text{if } Re_{p,r} > 0 \end{cases} \tag{14}$$

where $Y_r^H = 4e_{c,r}^5\left[-6e_{c,r}+3\left(1+e_{c,r}^2\right)\cdot\ln\left(\frac{1+e_{c,r}}{1-e_{c,r}}\right)\right]^{-1}$, $\bar{\bar{\boldsymbol{\varepsilon}}}$ is the Levi-Civita tensor, $\dot{\bar{\bar{\boldsymbol{\gamma}}}}_r = \dot{\gamma}_{jl,r} = \frac{1}{2}\left(\frac{\partial u_{j,r}}{\partial x_l}+\frac{\partial u_{l,r}}{\partial x_j}\right)$ is the velocity gradient tensor, and the operator : is defined such that:

$$\left(\bar{\bar{\boldsymbol{\varepsilon}}}\mathbf{o}_r\right):\left(\dot{\bar{\bar{\boldsymbol{\gamma}}}}_r\mathbf{o}_r\right)\Big|_i = \varepsilon_{ijk}\left(\dot{\gamma}_{jl,r}o_{l,r}\right)o_{j,r}.$$

5.2 Tridiagonal block matrix solution for the constraint equation

The connectivity constraint imposed by Eq. (5) can be also formulated as:

$$\frac{d\boldsymbol{\Psi}}{dt} = \mathbf{0} \tag{15}$$

with initial condition $\boldsymbol{\Psi}(t=0)=\mathbf{0}$. After some algebra, the discretized form of Eq. (15) reads:

$$\mathbf{v}_r^{n+1} - \mathbf{v}_r^n - a\left(\lambda_{r+1}\bar{\bar{\mathbf{O}}}_{r+1}^n\boldsymbol{\omega}_{r+1}^{n+1} + \lambda_r\bar{\bar{\mathbf{O}}}_r^n\boldsymbol{\omega}_r^{n+1}\right) = \mathbf{0} \tag{16}$$

where:

$$\bar{\bar{\mathbf{O}}}_r^n = \begin{bmatrix} 0 & -o_{z;r}^n & o_{y;r}^n \\ o_{z;r}^n & 0 & -o_{x;r}^n \\ -o_{y;r}^n & o_{x;r}^n & 0 \end{bmatrix} \implies \mathbf{o}_r^n \times \mathbf{x} = \bar{\bar{\mathbf{O}}}_r^n\mathbf{x} \quad \forall\mathbf{x}\in R^3; \tag{17}$$

$$\mathbf{v}_r^{n+1} = \mathbf{K}_r^n + \bar{\bar{\mathbf{Q}}}_r^n\left(\mathbf{X}_{r+1}^n - \mathbf{X}_r^n\right); \tag{18}$$

$$\boldsymbol{\omega}_r^{n+1} = \mathbf{R}_r^n + \bar{\bar{\mathbf{S}}}_r^n\left(\mathbf{X}_{r+1}^n + \mathbf{X}_r^n\right); \tag{19}$$

$$\mathbf{p}_r^{n+1} = \mathbf{p}_r^n + \Delta t\mathbf{v}_r^{n+1}; \tag{20}$$

$$\mathbf{o}_r^{n+1} = \mathbf{o}_r^n - \Delta t\bar{\bar{\mathbf{O}}}_r^n\boldsymbol{\omega}_r^{n+1} \tag{21}$$

with:

$$\begin{aligned}
\mathbf{K}_r^n &= \left(\bar{\bar{\boldsymbol{\delta}}} + \frac{\Delta t}{m_p}\bar{\bar{\mathbf{A}}}_r^n\right)^{-1}\left(\mathbf{v}_r^n + \frac{\Delta t}{m_p}\bar{\bar{\mathbf{A}}}_r^n\mathbf{u}_r^n\right);\\
\bar{\bar{\mathbf{Q}}}_r^n &= \frac{\Delta t}{m_p}\left(\bar{\bar{\boldsymbol{\delta}}} + \frac{\Delta t}{m_p}\bar{\bar{\mathbf{A}}}_r^n\right)^{-1};\\
\mathbf{R}_r^n &= \left(\bar{\bar{\mathbf{J}}}_n^r + \Delta t\bar{\bar{\mathbf{C}}}_r^n\right)^{-1}\left[\bar{\bar{\mathbf{J}}}_r^n\boldsymbol{\omega}_r^n + \Delta t\left(\dot{\bar{\bar{\mathbf{J}}}}_r^n\boldsymbol{\omega}_r^n + \bar{\bar{\mathbf{C}}}_r^{n+1}\boldsymbol{\Omega}_r^n + \mathbf{H}_r^D\right)\right];\\
\bar{\bar{\mathbf{S}}}_r^n &= \lambda_r a\left(\bar{\bar{\mathbf{J}}}_n^r + \Delta t\bar{\bar{\mathbf{C}}}_r^n\right)^{-1}.
\end{aligned}$$

Adopting the following definitions:

$$\mathbf{K}_n^{tot} = -\mathbf{K}_{r+1}^n + \mathbf{K}_r^n - a\left(\lambda_r\bar{\bar{\mathbf{O}}}_r^n\mathbf{R}_r^n + \lambda_{r+1}\bar{\bar{\mathbf{O}}}_{r+1}^n\mathbf{R}_{r+1}^n\right); \tag{22}$$

$$\bar{\bar{\mathbf{M}}}_r^n = \bar{\bar{\mathbf{Q}}}_r^n + \lambda_r a\bar{\bar{\mathbf{O}}}_r^n\bar{\bar{\mathbf{S}}}_r^n\bar{\bar{\mathbf{O}}}_r^n; \tag{23}$$

$$\bar{\bar{\mathbf{N}}}_r^n = -\bar{\bar{\mathbf{Q}}}_r^n + \lambda_r a\bar{\bar{\mathbf{O}}}_r^n\bar{\bar{\mathbf{S}}}_r^n\bar{\bar{\mathbf{O}}}_r^n \tag{24}$$

the constraint equation can be rewritten as:

$$\bar{\bar{\mathbf{M}}}_{r+1}^n\mathbf{X}_{r+2}^n + \underbrace{\left(\bar{\bar{\mathbf{N}}}_{r+1}^n + \bar{\bar{\mathbf{N}}}_r^n\right)}_{\bar{\bar{\mathbf{N}}}_{r,r+1}^n}\mathbf{X}_{r+1}^n + \bar{\bar{\mathbf{M}}}_r^n\mathbf{X}_r^n = \mathbf{K}_r^n. \tag{25}$$

In matrix form, it reads:

$$\underbrace{\begin{bmatrix} \mathbf{N}^n_{1,2} & \mathbf{M}^n_2 & \mathbf{0} & \dots & \dots & \mathbf{0} \\ \mathbf{M}^n_2 & \mathbf{N}^n_{2,3} & \mathbf{M}^n_3 & \mathbf{0} & \dots & \mathbf{0} \\ \dots & \dots & \dots & \dots & \dots & \dots \\ \mathbf{0} & \dots & \mathbf{0} & \mathbf{M}^n_{\mathcal{N}-2} & \mathbf{N}^n_{\mathcal{N}-2,\mathcal{N}-1} & \mathbf{M}^n_{\mathcal{N}-1} \\ \mathbf{0} & \dots & \dots & \mathbf{0} & \mathbf{M}^n_{\mathcal{N}-1} & \mathbf{N}^n_{\mathcal{N}-1,\mathcal{N}} \end{bmatrix}}_{\mathcal{M}} \underbrace{\begin{Bmatrix} \mathbf{X}^n_2 \\ \mathbf{X}^n_3 \\ \vdots \\ \mathbf{X}^n_{\mathcal{N}-1} \\ \mathbf{X}^n_{\mathcal{N}} \end{Bmatrix}}_{\mathcal{X}} = \underbrace{\begin{Bmatrix} \mathbf{K}^n_2 \\ \mathbf{K}^n_3 \\ \vdots \\ \mathbf{K}^n_{\mathcal{N}-1} \\ \mathbf{K}^n_{\mathcal{N}} \end{Bmatrix}}_{\mathcal{K}}. \tag{26}$$

This tridiagonal block matrix system can be solved using an exact method. In this study, we adopted the $\mathcal{LU}$ factorization because of its simplicity and ease of implementation. The tridiagonal block matrix $\mathcal{M}$ is decomposed into a lower and an upper diagonal block matrix, $\mathcal{L}$ and $\mathcal{U}$, respectively:

$$\mathcal{M} = \underbrace{\begin{bmatrix} \bar{\bar{\mathbf{L}}}^n_1 & \mathbf{0} & \dots & \dots & \dots \\ \bar{\bar{\mathbf{M}}}^n_2 & \bar{\bar{\mathbf{L}}}^n_2 & \mathbf{0} & \dots & \dots \\ \dots & \dots\dots & \dots & \dots & \dots \\ \dots & \dots\dots & \dots & \dots & \dots \\ \dots & \dots & \mathbf{0} & \bar{\bar{\mathbf{M}}}^n_{\mathcal{N}-1} & \bar{\bar{\mathbf{L}}}_{\mathcal{N}} \end{bmatrix}}_{\mathcal{L}} \underbrace{\begin{bmatrix} \bar{\bar{\delta}} & \bar{\bar{\mathbf{U}}}^n_1 & \mathbf{0} & \dots\dots \\ \mathbf{0} & \bar{\bar{\delta}} & \bar{\bar{\mathbf{U}}}^n_2 & \mathbf{0} & \dots \\ \dots & \dots & \dots & \dots & \dots \\ \dots & \dots & \dots & \dots & \dots \\ \dots & \dots & \dots & \mathbf{0} & \bar{\bar{\delta}} \end{bmatrix}}_{\mathcal{U}} \tag{27}$$

where:

$$\begin{aligned} &\bar{\bar{\mathbf{L}}}^n_1 = \bar{\bar{\mathbf{N}}}^n_{1,2}; \\ &\bar{\bar{\mathbf{U}}}^n_1 = \left(\bar{\bar{\mathbf{N}}}^n_{1,2}\right)^{-1} \bar{\bar{\mathbf{M}}}_2; \\ &\bar{\bar{\mathbf{L}}}^n_r = \bar{\bar{\mathbf{N}}}^n_{r,r+1} - \bar{\bar{\mathbf{M}}}^n_r \bar{\bar{\mathbf{U}}}^n_{r-1} \qquad \text{if } r \in [2, \mathcal{N}]; \\ &\bar{\bar{\mathbf{U}}}^n_r = \left(\bar{\bar{\mathbf{L}}}^n_r\right)^{-1} \bar{\bar{\mathbf{M}}}^n_{r+1} \qquad \text{if} \quad r \in [2, \mathcal{N}-1] \ . \end{aligned} \tag{28}$$

The system Eq. (26) is now equivalent to:

$$\mathcal{L} \underbrace{\mathcal{U} \mathcal{X}}_{\mathcal{Y}} = \mathcal{K} \quad \Longleftrightarrow \quad \begin{cases} \mathcal{L}\mathcal{Y} = \mathcal{K} \\ \mathcal{U}\mathcal{X} = \mathcal{Y}. \end{cases} \tag{29}$$

We thus obtain:

$$\begin{aligned} &\mathbf{y}^n_1 = \left(\bar{\bar{\mathbf{N}}}^n_{1,2}\right)^{-1} \mathbf{K}^n_1; \\ &\mathbf{y}^n_r = \left(\bar{\bar{\mathbf{L}}}^n_r\right)^{-1} \left[\mathbf{K}^n_r - \bar{\bar{\mathbf{M}}}^n_r \mathbf{y}^n_{r-1}\right] \qquad if \ r \in [2, \mathcal{N}]; \\ &\mathbf{X}^n_{\mathcal{N}} = \mathbf{y}^n_{\mathcal{N}}; \\ &\bar{\bar{\mathbf{U}}}^n_r = \left(\bar{\bar{\mathbf{L}}}^n_r\right)^{-1} \bar{\bar{\mathbf{M}}}^n_{r+1} \qquad \text{if} \quad r \in [2, \mathcal{N}-1] \ . \end{aligned} \tag{30}$$

References

1. Andersson, H.I., Zhao, L., Barri, M.: Torque-coupling and particle-turbulence interactions. J. Fluid Mech. **696**, 319 (2012)
2. Andrić, J., Fredriksson, S.T., Lindström, S.B., Sasic, S., Nilsson, H.: A study of a flexible fiber model and its behavior in DNS of turbulent channel flow. Acta Mech. **224**, 2359 (2013)
3. Andrić, J., Lindström, S.B., Sasic, S., Nilsson, H.: Rheological properties of dilute suspensions of rigid and flexible fibers. J. Non-Newton. Fluid Mech. **212**, 36 (2014)
4. Boer, L., Buist, K.A., Deen, N.G., Padding, J.T., Kuipers, J.A.M.: Experimental study on orientation and de-mixing phenomena of elongated particles in gas-fluidized beds. Powder Technol. **329**, 332 (2018)

5. Brenner, H., Cox, R.G.: The resistance to a particle of arbitrary shape in translational motion at small Reynolds numbers. J. Fluid Mech. **17**, 561 (1963)
6. Brenner, H.: The Stokes resistance of an arbitrary particle IV. Arbitrary fields of flow. Chem. Eng. Sci. **19**, 703 (1964)
7. Brouzet, C., Verhille, G., Le Gal, P.: Flexible fiber in a turbulent flow: a macroscopic polymer. Phys. Rev. Lett. **112**, 074501 (2014)
8. Byron, M., Einarsson, J., Gustavsson, K., Voth, G., Mehlig, B., Variano, E.: Shape-dependence of particle rotation in isotropic turbulence. Phys. Fluids **27**, 035101 (2015)
9. Challabotla, N.R., Zhao, L., Andersson, H.I.: Orientation and rotation of inertial disk particles in wall turbulence. J. Fluid Mech. **766**, R2 (2015)
10. Clift, R., Grace, J.R., Weber, M.E.: Bubbles, Drops and Particles. Academic Press, New York (1978)
11. Cox, R.G.: The motion of long slender bodies in a viscous fluid. Part 2. Shear flow. J. Fluid Mech. **45**, 625 (1971)
12. De Lillo, F., Cencini, M., Durham, W.M., Barry, M., Stocker, R., Climent, E., Boffetta, G.: Turbulent fluid acceleration generates clusters of gyrotactic microorganisms. Phys. Rev. Lett. **112**, 044502 (2014)
13. Delmotte, B., Climent, E., Plouraboué, F.: A general formulation of bead models applied to flexible fibers and active filaments at low Reynolds number. J. Comput. Phys. **286**, 14 (2015)
14. Dong, S., Feng, X., Salcudean, M., Gartshore, I.: Concentration of pulp fibers in 3D turbulent channel flow. Int. J. Multiph. Flow **29**, 1 (2003)
15. Do-Quang, M., Amberg, G., Brethouwer, G., Johansson, A.V.: Simulation of finite-size fibers in turbulent channel flows. Phys. Rev. E **89**, 013006 (2014)
16. Eshghinejadfard, A., Hosseini, S.A., Thévenin, D.: Fully-resolved prolate spheroids in turbulent channel flows: a lattice Boltzmann study. AIP Adv. **7**, 095007 (2017)
17. Eshghinejadfard, A., Sharma, K., Thévenin, D.: Effect of polymer and fiber additives on pressure drop in a rectangular channel. J. Hydrodyn. B **29**, 871 (2017)
18. Fan, F.G., Ahmadi, G.: A sublayer model for wall deposition of ellipsoidal particles in turbulent streams. J. Aerosol Sci. **25**, 831 (1995)
19. Gallily, I., Cohen, A.H.: On the orderly nature of the motion of non-spherical aerosol particles. II. Inertial collision between a spherical large droplet and axially symmetrical elongated particle. J. Colloid Interface Sci. **68**, 338 (1979)
20. Gustavsson, K., Jucha, J., Naso, A., Lévêque, E., Pumir, A., Mehlig, B.: Statistical model for the orientation of non-spherical particles settling in turbulence. Phys. Rev. Lett. **119**, 254501 (2017)
21. Hich, E.J., Leal, L.G.: Rotation of small non-axisymmetric particles in a simple shear flow. J. Fluid Mech. **92**, 591 (1979)
22. Huang, W.X., Shin, S.J., Sung, H.J.: Simulation of flexible filaments in a uniform flow by the immersed boundary method. J. Comput. Phys. **226**, 2206 (2007)
23. Jeffery, G.B.: The motion of ellipsoidal particles immersed in a viscous fluid. Proc. R. Soc. Lond. Ser. A **102**, 161 (1922)
24. Joung, C.G., Phan-Thien, N., Fan, X.J.: Direct simulation of flexible fibers. J. Non-Newton. Fluid Mech. **99**, 1 (2001)
25. Kim, S., Karrila, S.J.: Microhydrodynamics: Principles and Selected Applications. Butterworth-Heinemann, Stoneham (1991)
26. Kunhappan, D., Harthong, B., Chareyre, B., Balarac, G., Dumont, P.J.J.: Numerical modelling of high aspect ratio flexible fibers in inertial flows. Phys. Fluids **29**, 093302 (2017)
27. Lindström, S.B., Uesaka, T.: Particle-level simulation of forming of the fiber network in papermaking. Int. J. Eng. Sci. **46**, 858 (2008)
28. Lindström, S.B., Uesaka, T.: Simulation of the motion of flexible fibers in viscous fluid flow. Phys. Fluids **19**, 113307 (2007)
29. Lopez, D., Guazzelli, E.: Inertial effects on fibers settling in a vortical flow. Phys. Rev. Fluids **2**, 024306 (2017)
30. López, H.M., Hulin, J.-P., Auradou, H., D'Angelo, M.V.: Deformation of a flexible fiber in a viscous flow past an obstacle. Phys. Fluids **27**, 013102 (2015)
31. Lovecchio, S., Zonta, F., Marchioli, C., Soldati, A.: Thermal stratification hinders gyrotactic micro-organism rising in free-surface turbulence. Phys. Fluids **29**, 053302 (2017)
32. Lovecchio, S., Marchioli, C., Soldati, A.: Time persistence of floating particle clusters in free-surface turbulence. Phys. Rev. E **88**, 033003 (2013)
33. Lundell, F., Soderberg, L.D., Alfredsson, P.H.: Fluid mechanics of papermaking. Annu. Rev. Fluid Mech. **43**, 195 (2011)
34. Marchioli, C.: Large-eddy simulation of turbulent dispersed flows: a review of modelling approaches. Acta Mech. **228**, 741 (2017)
35. Marchioli, C., Zhao, L., Andersson, H.I.: On the relative rotational motion between rigid fibers and fluid in turbulent channel flow. Phys. Fluids **28**, 013301 (2016)
36. Marchioli, C., Soldati, A.: Rotation statistics of fibers in wall shear turbulence. Acta Mech. **224**, 2311 (2013)
37. Marchioli, C., Fantoni, M., Soldati, A.: Orientation, distribution, and deposition of elongated, inertial fibers in turbulent channel flow. Phys. Fluids **22**, 033301 (2010)
38. Marchioli, C., Soldati, A.: Mechanism for particle transfer and segregation in turbulent boundary layer. J. Fluid Mech. **468**, 283 (2002)
39. Martínez, M., Vernet, A., Pallares, J.: Clustering of long flexible fibers in two-dimensional flow fields for different Stokes numbers. Int. J. Heat Mass Transf. **111**, 532 (2017)
40. Maxey, M.: Simulation methods for particulate flows and concentrated suspensions. Annu. Rev. Fluid Mech. **49**, 171 (2017)
41. Moffet, R.C., Prater, K.A.: In-situ measurements of the mixing state and optical properties of soot with implications for radiative forcing estimates. Proc. Natl. Acad. Sci. **106**, 11872 (2009)
42. Niazi Ardekani, M., Sardina, G., Brandt, L., Karp-Boss, L., Bearon, R.N., Variano, E.A.: Sedimentation of inertia-less prolate spheroids in homogenous isotropic turbulence with application to non-motile phytoplankton. J. Fluid Mech. **831**, 655 (2017)
43. Niazi Ardekani, M., Costa, P., Breugem, W.-P., Picano, F., Brandt, L.: Drag reduction in turbulent channel flow laden with finite-size oblate spheroids. J. Fluid Mech. **816**, 43 (2017)
44. Parsa, S., Calzavarini, E., Toschi, F., Voth, G.A.: Rotation rate of rods in turbulent fluid flow. Phys. Rev. Lett. **109**, 134501 (2012)

45. Pei, Z., Zhang, Y., Zhou, J.: A model for the particle-level simulation of multiple flexible fibers moving in a wall-bounded fluid flow. J. Fluids Struct. **80**, 37 (2018)
46. Picciotto, M., Marchioli, C., Soldati, A.: Characterization of near-wall accumulation regions for inertial particles in turbulent boundary layers. Phys. Fluids **17**, 098101 (2005)
47. Quennouz, N., Shelley, M., Du Roure, O., Lindner, A.: Transport and buckling dynamics of an elastic fibre in a viscous cellular flow. J. Fluid Mech. **769**, 387 (2015)
48. Ravnik, J., Marchioli, C., Soldati, A.: Application limits of Jeffery's theory for elongated particle torques in turbulence: a DNS assessment. Acta Mech. **229**, 827 (2018)
49. Rosén, T., Do-Quang, M., Aidun, C.K., Lundell, F.: Effect of fluid and particle inertia on the rotation of an oblate spheroidal particle suspended in linear shear flow. Phys. Rev. E **91**, 053017 (2015)
50. Ross, R.F., Klingenberg, D.J.: Dynamic simulation of flexible fibers composed of linked rigid bodies. J. Chem. Phys. **106**, 2949 (1997)
51. Sabban, L., Cohen, A., van Hout, R.: Temporally resolved measurements of heavy, rigid fibre translation and rotation in nearly homogeneous isotropic turbulence. J. Fluid Mech. **814**, 42 (2017)
52. Sabban, L., van Hout, R.: Measurements of pollen grain dispersal in still air and stationary, near homogeneous, isotropic turbulence. J. Aerosp. Sci. **42**, 867 (2011)
53. Sasayama, T., Inagaki, M.: Simplified bead-chain model for direct fiber simulation in viscous flow. J. Nonnewton. Fluid Mech. **250**, 52 (2017)
54. Schmid, C.F., Switzer III, L.H., Klingenberg, D.J.: Simulations of fiber flocculation: effects of fiber properties and inter-fiber friction. J. Rheol. **44**, 781 (2000)
55. Shams, M., Ahmadi, G., Rahimzadeh, H.: Transport and deposition of flexible fibers in turbulent duct flows. J. Aerosol Sci. **32**, 525 (2001)
56. Shapiro, M., Goldenberg, M.: Deposition of glass fiber particles from turbulent air flow in a pipe. J. Aerosol Sci. **24**, 65 (1993)
57. Slowicka, A.M., Wajnryb, E., Ekiel-Jezewska, M.L.: Dynamics of flexible fibers in shear flow. J. Chem. Phys. **143**, 124904 (2015)
58. Soldati, A., Marchioli, C.: Physics and modelling of turbulent particle deposition and entrainment: review of a systematic study. Int. J. Multiph. Flow **35**, 827 (2009)
59. Stockie, J.M., Green, S.I.: Simulating the motion of flexible pulp fibres using the immersed boundary method. J. Comput. Phys. **147**, 398 (1998)
60. Subramanian, G., Koch, D.L.: Inertial effects on fibre motion in simple shear flow. J. Fluid Mech. **535**, 383 (2005)
61. Switzer III, L.H., Klingenberg, D.J.: Rheology of sheared flexible fiber suspensions via fiber-level simulations. J. Rheol. **47**, 759 (2003)
62. Tang, Y., Wu, T.-H., He, G.-W., Qi, D.: Multi-flexible fiber flows: a direct-forcing immersed boundary lattice-Boltzmann lattice-spring approach. Int. J. Multiph. Flow **99**, 408 (2018)
63. Toschi, F., Bodenschatz, E.: Lagrangian properties of particles in turbulence. Annu. Rev. Fluid Mech. **41**, 375 (2009)
64. Vakil, A., Green, S.I.: Flexible fiber motion in the flow field of a cylinder. Int. J. Multiph. Flow **37**, 173 (2011)
65. Verhille, G., Bartoli, A.: 3D conformation of a flexible fiber in a turbulent flow. Exp. Fluids **57**, 117 (2016)
66. Voth, G.A., Soldati, A.: Anisotropic particles in turbulence. Annu. Rev. Fluid Mech. **49**, 249 (2017)
67. Vreman, A.W.: A staggered overset grid method for resolved simulation of incompressible flow around moving spheres. J. Comput. Phys. **333**, 269–296 (2017)
68. Wang, G., Yu, W., Zhou, C.: Optimization of the rod chain model to simulate the motions of a long flexible fiber in simple shear flows. Eur. J. Mech. B Fluids **44**, 337 (2006)
69. Wu, J., Aidun, C.K.: A method for direct simulation of flexible fiber suspensions using lattice Boltzmann equation with external boundary force. Int. J. Multiph. Flow **36**, 202 (2010)
70. Xiang, P., Kuznetsov, A.V.: Simulation of shape dynamics of a long flexible fiber in a turbulent flow in the hydro-entanglement process. Int. Commun. Heat Mass Transf. **35**, 529 (2008)
71. Yamamoto, S., Matsuoka, T.: A method for dynamic simulation of rigid and flexible fibers in a flow field. J. Chem. Phys. **98**, 644 (1993)
72. Yuan, W., Andersson, H.I., Zhao, L., Challabotla, N.R., Deng, J.: Dynamics of disk-like particles in turbulent vertical channel flow. Int. J. Multiph. Flow **96**, 86 (2017)
73. Zhao, L., Gustavsson, K., Ni, R., Kramel, S., Voth, G., Andersson, H.I., Mehlig, B.: Orientation patterns of non-spherical particles in turbulence. arXiv:1707.06037v2 [physics.flu-dyn]
74. Zhao, F., van Wachem, B.G.M.: Four-way coupled simulations of small particles in turbulent channel flow: the effects of particle shape and Stokes number. Phys. Fluids **27**, 083301 (2015)
75. Zhao, L., Marchioli, C., Andersson, H.I.: Slip velocity of rigid fibers in turbulent channel flow. Phys. Fluids **26**, 063302 (2014)
76. Zhao, F., George, W.K., van Wachem, B.G.M.: Direct numerical simulation of ellipsoidal particles in turbulent channel flow. Acta Mech. **224**, 2331 (2013)
77. Zhan, C., Sardina, G., Lushi, E., Brandt, L.: Accumulation of motile elongated micro-organisms in turbulence. J. Fluid Mech. **739**, 22 (2014)
78. Zhang, D., Smith, D.E.: Dynamic simulation of discrete fiber motion in fiber-reinforced composite materials processing. J. Compos. Mater. **50**, 1301 (2016)
79. Zhu, L., Peskin, C.S.: Drag of a flexible fiber in a 2D moving viscous fluid. Comput. Fluids **36**, 398 (2007)